

Photonic Integrated Circuits Fabricated Using Ion Implantation

Sylvain Charbonneau, Emil S. Koteles, *Member, IEEE*, P. J. Poole, J. J. He, G. C. Aers, J. Haysom, M. Buchanan, Y. Feng, A. Delage, F. Yang, M. Davies, R. D. Goldberg, P. G. Piva, and I. V. Mitchell

(Invited Paper)

Abstract— Intermixing the wells and barriers of quantum-well (QW) laser heterostructures generally results in an increase in the bandgap energy and is accompanied by changes in the refractive index. A technique, based on ion implantation-induced QW intermixing, has been developed to enhance the quantum-well intermixing (QWI) rate in selected areas of a wafer. Such processes offer the prospect of a powerful and simple fabrication route for the integration of discrete optoelectronic devices and for forming photonic integrated circuits.

Index Terms— Annealing, diffusion processes, interdiffusion processes, quantum wells, semiconductor devices.

I. INTRODUCTION

RAPID ADVANCES in optoelectronics (OE) are crucial for expediting the transition from the industrial age to the information age. For example, the development of semiconductor laser diodes and photodiodes was essential for the realization of cost-effective optical fiber communications networks. These optical fiber systems are in wide use today for both long haul and interoffice networks. Today, we are at the threshold of another revolutionary development, the integration of optical and electronic components into optoelectronic integrated circuits (OEIC) combining elements of both of these technologies.

The primary objectives of optoelectronic integration are similar to those of electronic integration: enhancing the performance, reliability and increasing the functionality while lowering the manufacturing cost. Over a period of thirty years, the electronics industry has moved from discrete transistors to very large-scale integrated circuits (VLSI), with which up to 20 million transistors can now be integrated on a single chip. The cost and reliability improvements achieved through these developments have been largely responsible for enabling all the advancements in electronic information transmission and processing. Integration is perhaps more important for optical systems than it was for electronic technologies, because one of the key attributes of optics is inherent parallelism, i.e.,

simultaneous operation at many wavelengths, as opposed to the serial nature of transistors. Like electronic integrated circuits, which involve the replication of huge numbers of components of various functionalities (transistors, diodes, resistors, capacitors, etc.), optoelectronic integration requires the integration of fundamentally different types of components, including some based on different materials. Generally, however, OE devices have been largely based on similar materials, typically III–V semiconductor materials, and are processed using many of the same technologies that form the basis for silicon integrated circuit fabrication. Optical components rely on both the optical and electronic properties of their constituent materials and they often require heteroepitaxially grown material with accurately controlled composition to achieve optimum performance. As a result, OEIC's are typically more complex in structure than silicon IC's. A further complication is that in their most versatile form, OEIC's are built up from components that are very different in functionality: light emitters, waveguides, modulators and detectors. Each of these different components may require different material structures to achieve optimized performance.

A distinction is sometimes made between OEIC's that incorporate only photonic components, i.e., photonic integrated circuits (PIC's), and those integrating both optical and electronic elements such as optical detectors with transistors. PIC's are a subset of OEIC's utilizing a single substrate for the monolithic integration of optically interconnected guided-wave optoelectronic devices. Most OEIC's fabricated to date have been aimed at applications fulfilling the needs of conventional point-to-point optical communications. Here, the optical device functions only as a terminal device to convert a processed electrical signal into an encoded optical signal for fiber transmission, or vice versa. In contrast, PIC's contain optically interconnected devices that reroute, condition, or process the signal while still in its optical form.

The driving force for the development of PIC's is the expected complexity of next-generation optical communications links, networking architectures, and even switching systems. The elaborate schemes currently being developed, including multichannel wavelength-division multiplexing (WDM), as well as high-speed time-division multiplexing (TDM), involve a great variety of optically cascaded emitters, modulators, filters, amplifiers, switches, detectors, etc. A large portion of the cost of such architectures is due to the difficulty

Manuscript received March 6, 1998; revised June 30, 1998.

S. Charbonneau, E. S. Koteles, P. J. Poole, J. J. He, G. C. Aers, J. Haysom, M. Buchanan, Y. Feng, A. Delage, F. Yang, and M. Davies are with the Institute for Microstructural Sciences, National Research Council of Canada, Ottawa, ON, K1A 0R6, Canada.

R. D. Goldberg, P. G. Piva, and I. V. Mitchell are with the Department of Physics, University of Western Ontario, London, ON, N6A 3K7, Canada.

Publisher Item Identifier S 1077-260X(98)06935-4.

of achieving single-mode optical connections between the guided-wave components. Such devices often require tightly confining waveguides for optimized performance, resulting in difficult submicrometer alignment tolerances when such structures are coupled to single-mode optical fibers. By replacing individually aligned connections with lithographically produced waveguides, PIC's offer the promise of cost reduction, dramatically reduced size, and increased packaging robustness.

A great variety of guided-wave devices have been investigated during the past two decades. This work has mostly been limited to the area of electrooptics and passive waveguide devices due, at least in part, to the relatively immature fabrication technology associated with optical sources and detectors. Only within the past few years have semiconductor crystal growth and processing techniques advanced to the point where integrated optical component concepts may be contemplated. Among these advances are the large area uniformity and reproducibility of growth offered by the current generation of vapor and beam growth techniques such as metal-organic vapor phase epitaxy (MOVPE) and chemical beam epitaxy (CBE). Especially in the InGaAsP-InP system, of interest for its telecommunications applications, highly complex vertical layer structures including large numbers of thin etch-stop layers have ushered in a dramatic new level of design and fabrication freedom in the engineering of semiconductor guided-wave devices.

This article is about one key technological challenge in expanding the versatility and functionality of optoelectronics: research aimed at the integration of multiple-function devices onto a single substrate. The paper will outline the work presently underway within the Institute for Microstructural Sciences (IMS) of the National Research Council of Canada, in collaboration with the University of Western Ontario (UWO) and Canadian industry, on ion-implantation-induced quantum-well intermixing (QWI) in III-V-based heterostructures for the realization of practical PIC's. The paper is divided into three sections. In the first part, the criteria needed for the practical integration of OE devices will be reviewed and the various approaches for monolithic photonic integration based on QW active layers will be described. The second part will concentrate on the use of ion-implantation-induced QWI as an integration technique. Finally, some illustrative examples of prototype devices from the authors' own current research, will be discussed to give a broader view of potential application areas.

II. CRITERIA AND TECHNIQUES FOR MONOLITHIC PHOTONIC INTEGRATION

Practicality mandates low manufacturing cost and high reliability (low operating cost) of commercial PIC devices, even at the expense of somewhat reduced performance. With this in mind, we can establish the most important requirement for monolithically integrating optoelectronic devices of differing functionalities in order to achieve practical waveguiding PIC's. We will concern ourselves here only with waveguiding PIC's, in which the signal carrying optical beam is confined within a waveguide near the surface of a wafer. All signal processing takes place in this plane. This is believed to be the most likely form for monolithic PIC's, as waveguide optical modes are

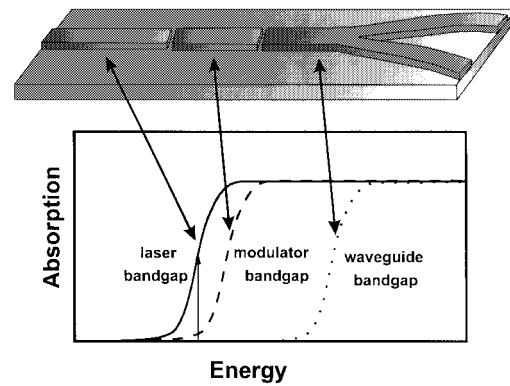


Fig. 1. Schematic diagram of a "generic" PIC containing a laser diode whose output is directed into a transparent waveguide 3-dB splitter through an external electroabsorptive modulator. The optimum operation of this PIC requires that the bandgap energies of these three components possess the specific relationship illustrated in the figure.

the most compatible with optical fibers and on-chip optical signal processing.

The primary requirement for waveguiding PIC's is bandgap compatibility among the various optoelectronic devices, as illustrated schematically in Fig. 1 for a "generic" PIC. In such PIC's, the signal carrying light beam is directed by passive, transparent, optical waveguides to various active optoelectronic devices in the plane of the wafer. Optimum performance demands that the bandgap energies of the various components be related to each other in a specific fashion. For example, in Fig. 1, it is essential that the passive waveguide collecting and distributing the light from the laser diode be as transparent as possible to the laser wavelength (i.e., have a larger bandgap energy than that of the laser structure) so that a minimum amount of optical power is lost to absorption during transit. On the other hand, the external electroabsorptive modulator (a quantum confined Stark effect (QCSE) modulator—essentially a reverse biased laser structure) should have a slightly larger bandgap than the laser to achieve optimum operating parameters (low loss and good contrast). The advantage of even such a simple PIC lies in the increased operational bandwidth, reduced chirp, and possibly reduced demands on the drive circuits that external modulation provides.

The realization of PIC's requires spatially selective control over the optical and electrical characteristics of the multiple quantum well material. Several approaches to integration based on QW active layers are emerging. The first, is based on regrowth and involves growing a structure containing the QW active layers for all the devices [1]. The active layers are then etched from the regions where they are not needed and the structure is overgrown with the same upper cladding layers everywhere. In the event that more than one set of active layer QW's is required, they can be grown on top of each other and the structure designed so that light couples vertically from one layer to the other. This technique imposes severe limitations on device performance because in some part of the PIC, current must be applied to several active layers in series. Furthermore, regrowth techniques require complex technologies such as MOVPE during the entire production process, leading to low production yield.

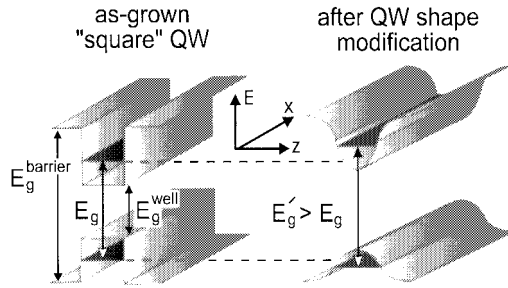


Fig. 2. Schematic diagram illustrating the effect of QW shape modification on QW bandgap energies.

A second technique used for integration is selective area epitaxy, also known as “growth on a patterned substrate,” where the width of the QW’s can be varied across the wafer during a single growth [2].¹ In this approach, the substrate is usually coated with a dielectric mask (such as SiO_2) in which slots are opened. Under a precise set of growing conditions, no growth takes place on top of the dielectric, but surface migration of the group-III species (indium) can take place for some distance across the mask to the nearest opening. The growth rate in the opened area depends on the width of the opening and the patterning on the mask. This process works well for some applications, but is difficult to control and manipulate in more general situations. Another form of this technique is epitaxial growth on faceted mesas which makes use of the different surface diffusion lengths of deposited atomic species on different crystal facets [3].

A third technique, which is generating considerable interest due to its simplicity, is emerging as a powerful technique for fabricating PIC’s: QWI [4]. In this technique, the bandgap of a QW structure is modified selectively, after growth, by intermixing the well and barrier materials to form an alloy. This mechanism is based on the fact that a QW is an inherently metastable system due to the large concentration gradient of atomic species across the QW/barrier interface. For example, in InGaAs–InGaAsP QW’s, the phosphorus concentration changes from 43% to 0% (for layers lattice-matched to InP) in a distance of less than 1 nm. At temperatures above 750 °C significant diffusion of atomic species will occur resulting in an interdiffusion of the QW and barrier materials, as shown schematically in Fig. 2.

This process causes a rounding of the initially square QW bandgap profile and, in general, results in an increase of the bandgap energy. This provides a route to fabricating low-loss optical waveguides, and bandgap-shifted QCSE modulators, lasers and detectors, using only one epitaxial step. In addition, because the bandgap is increased, the refractive index is modified enough to provide optical confinement, gratings and laser reflectors. An example of using such refractive index changes will be provided in the next section.

This intermixing process can be greatly enhanced by the presence of impurities or defects in the vicinity of the interfaces of the QW, allowing intermixing to occur at temperatures that are substantially lower than that normally required. A

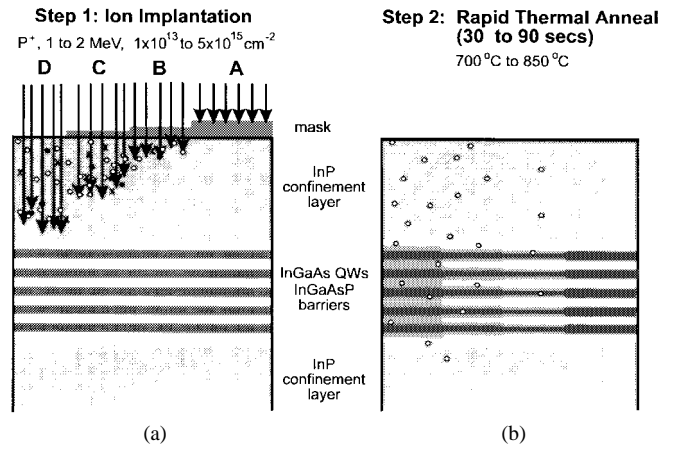


Fig. 3. Two-step process for achieving four different QW bandgap energies on a single wafer using a variable thickness mask and a single ion implantation. (a) Step 1: Standard ion implantation is performed through an SiO_2 photolithographic mask with four thicknesses thereby spatially altering the defect concentration created. (b) Step 2: After the mask is removed, a single rapid thermal anneal drives in vacancies and interstitials thereby enhancing thermally driven well/barrier interdiffusion.

number of intermixing techniques such as impurity induced disordering [5]–[7], laser beam induced disordering [8], impurity free vacancy diffusion [9]–[11] and ion-implantation-enhanced interdiffusion [12]–[14] have been utilized to enhance the thermally driven interdiffusion. All these techniques are spatially selective, permitting intermixing enhancement only in the regions requiring a larger bandgap, leaving other regions unmodified. In addition, they use standard QW structures and require no special growth processes. In the work at IMS and UWO being reviewed in this paper, ion implantation has been used to create controlled levels of defects in regions of the wafer that need to be modified. The two step process is illustrated schematically in Fig. 3 and extensive details can be found elsewhere [15]–[17].

To be practical, any monolithic photonic integration technique must fulfill several requirements.

- 1) There must be large, controllable bandgap energy differences between the various devices in the PIC.
- 2) Loss in the integrated waveguide devices must be comparable to or lower than that present in the as-grown (i.e., unmodified) structure.
- 3) The electrical properties of the various devices must suffer zero or insignificant deterioration due to the processing technique.
- 4) There should be no substantial adverse effects on the operating lifetimes of the various devices in the PIC, after processing.
- 5) Any other process-initiated changes in the properties of the devices must be either neutral or advantageous to the PIC.

We have demonstrated that spatially selective QW bandgap energy shifting due to QW shape modification fulfills these requirements.

The results presented below are primarily based on experiments performed on InP-based QW p-i-n laser structures, incorporating either lattice-matched or compressively strained QW’s fabricated from InGaAsP layers of various composi-

¹ For a review of this and other monolithic integration techniques, see, e.g., [2].

tions. Ion implantation was accomplished using the 1.7 MV Tandetron accelerator at the University of Western Ontario under a variety of implantation conditions (varying ion species, ion energy, dose and current, substrate temperature, etc.). Subsequent rapid thermal annealing (RTA) was performed at IMS, again under a variety of conditions in order to optimize the technique.

III. THE CONTROL OF ION-IMPLANTATION-INDUCED QWI

A. Parameters Affecting the Bandgap Energy Shifts in QWI

A common technique used to monitor QW shape modification, and therefore to characterize the effects of intermixing, is low-temperature (4.2 K) photoluminescence (PL) spectroscopy. This technique was used extensively in our work. The QW PL emission peak energy observed in these structures is directly related to the QW bandgap energy. After intermixing, the net PL energy shift is usually dominated by the change in bandgap at the center of the QW rather than the change in electron and hole confinement and is thus usually a blue shift (increasing the gap).

A number of parameters are important in determining the maximum bandgap energy shift one can obtain from a QW heterostructure. The QW blue shift increases with the interdiffusion length over which the disordering takes place. First and foremost, the design of the QW heterostructure itself can influence the magnitude of the blue shift. Three main factors have to be taken into account to tailor the energy shifts:

- 1) the difference in bandgap energy between the QW material and the barrier material;
- 2) the thickness of the QW;
- 3) the amount of strain present in the QW and barrier materials.

The effects of the bandgap shifting for each of these structural conditions have previously been studied in detail elsewhere [18]. In general, however, the larger the difference between the QW and barrier bandgap, the larger the expected blue shift for similar intermixing conditions; the thinner the QW width (down to about 3.0 nm) the larger the blue shift one can expect. For very narrow QW's, blue shifting actually decreases since quantized electronic levels in such wells are close to the "top" and must remain within the wells no matter how shallow they become due to the rules governing quantization. Thus there is little scope for movement of the levels and so little possibility of blue shifting [19]. Finally, the effect of strain (compressive versus lattice matched versus tensile) present on the various layers, is found to be a second order effect in the magnitude of the shift. The primary effect is the change in unstrained gap due to the change in composition at the center of the well.

For a given QW potential, the diffusion length can be increased by exposing the heterostructure to higher annealing temperatures or by using longer annealing times, which could lead to detrimental effects. In general, the annealing temperature and time for a given heterostructure is chosen such that blue shifting due to thermal intermixing in the absence of enhancement is very small.

The selective intermixing of QW layers at up to micron depths can be enhanced by ion implantation followed by rapid thermal annealing. The prevailing view is that the ion beam generates point defects (such as vacancies and interstitials) which promote intermixing of the QW region. In particular, the role of group-III vacancies has received substantial attention [20]. Most semiconductor devices require pristine crystallinity. Ion-implantation related damage is thus undesirable and has to be removed by thermal annealing. This process, which is based on the thermal diffusion of vacancies and interstitials, is also accompanied by the exchange of atoms across interfaces. Furthermore, compound semiconductors (binaries, ternaries, etc.) may have the tendency to undergo stoichiometric changes due to differences in diffusivities and volatility of some constituents. These processes are, obviously, undesirable and need to be suppressed. Schemes commonly employed to anneal such materials make use of rapid thermal annealing, in which the specimen is rapidly heated in an inert atmosphere, with the surface protected against effusion by proximity caps. Typical annealing conditions for III-V material systems are rapid heating to 700 °C–900 °C for times ranging from 0.1 to 3 min. Such annealing conditions seem to be adequate in restoring crystallinity, as the full PL intensity is usually recovered following annealing.

The number of point defects introduced in the heterostructures during the implantation process depends on many factors:

- 1) dose or fluence (number of ions/cm²);
- 2) masses of the ions (ion species),
- 3) angle at which the implantation is performed;
- 4) ion energy;
- 5) ion flux or current density (A/cm²);
- 6) temperature of the substrate during implantation.

Three examples are extracted from previously published work to demonstrate the importance of the implantation parameters.

The geometries of all heterostructures which will be discussed in the present article are shown schematically in Fig. 4 [13]. They represent standard laser design structures for 980- and 1.55- μm operation, and would be similar to future PIC designs. These "active" device structures contain the necessary waveguiding characteristics needed for monolithic integration. The examples shown here incorporate a series of InGaAs QW's. They consist essentially of (a) InGaAs–GaAs QW's embedded in Al_{0.70}Ga_{0.30}As cladding layers; and (b) InGaAs–InGaAsP QW's embedded in InP cladding layers. In these two structures, the QW's are at approximately the same depth from the surface (about 1.85 μm) and the cladding layers, through which the defects created by implantation have to diffuse, are of comparable width.

To demonstrate the importance of ion dose on the intermixing process, high energy (5 MeV) implantation was used to ensure that the expected ion range was greater than the depth of the QW's from the surface, therefore creating vacancies in and around the QW's. Fig. 5 presents the PL peak wavelength shift as a function of P⁺ dose, demonstrating that significant bandgap energy shifts are possible using this technique [15].

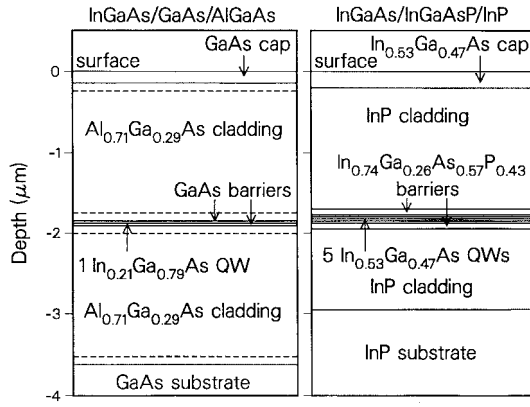


Fig. 4. Schematic diagrams of the InGaAs–GaAs–AlGaAs sample (left panel), which consists of a gradient index separate-confinement heterostructure (GRINSCH) laser structure containing a strained single 6.5-nm-wide InGaAs QW in a GaAs active region clad with AlGaAs. In the GRINSCH structure, the grading regions at the boundaries of each AlGaAs cladding layer are indicated by dashed lines. The InGaAs–InGaAsP–InP sample (right panel) is an unstrained laser structure containing five InGaAs QW in an InGaAsP active region clad with InP. The QW thicknesses are 6.0 nm.

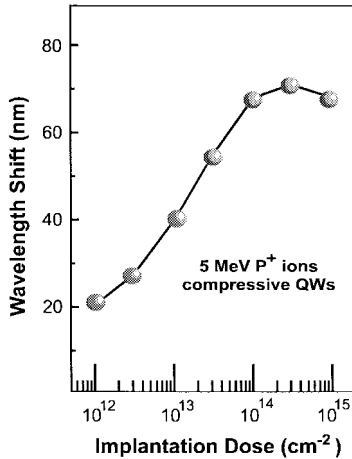


Fig. 5. QW PL peak wavelength change as a function of ion implantation dose for a compressively strained InP-based 5-nm-wide QW.

Another important implantation parameter is the energy at which the implantation is performed, i.e., the initial depth distribution of ion-induced damage prior to annealing is critical to the intermixing process and to the diffusion of defects through the different cladding materials. These issues were examined in both GaAs- and InP-based material systems using the layer structures shown in Fig. 4. Ion implantation was performed at various energies (ranging from 300 keV to 8.6 MeV) with the sample normal tilted 7° to the beam to avoid channeling [21]. For both structures, the ion species were chosen to avoid doping the structure: As^+ for the InGaAs–GaAs–AlGaAs sample and P^+ for the InGaAs–InGaAsP–InP sample. After implantation, the samples were annealed at 850°C and 700°C , respectively, for 30 s in a nitrogen atmosphere. In recent studies [22], these temperatures were found to produce significant intermixing of QW's in implanted regions of the samples without causing significant intermixing in the unimplanted regions.

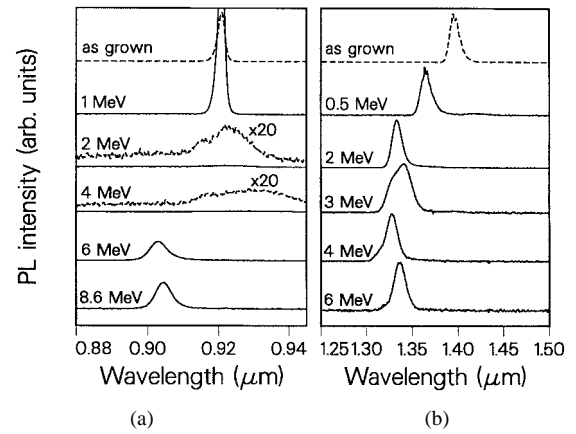


Fig. 6. PL emission spectra from (a) single strained $\text{In}_{0.21}\text{Ga}_{0.79}\text{As}$ –GaAs QW in the InGaAs–GaAs–AlGaAs laser structure and from (b) five unstrained $\text{In}_{0.53}\text{Ga}_{0.47}\text{As}$ – $\text{In}_{0.74}\text{Ga}_{0.26}\text{As}_{0.57}\text{P}_{0.43}$ QW's in the InGaAs–InGaAsP–InP laser structure. Spectra are given for typical as-grown samples (dashed lines) together with the results obtained after implantation with (a) arsenic ions and (b) phosphorous ions at the indicated energies, followed by 30-s anneal at 850°C and 700°C , respectively. In (a), the QW peak intensity has been normalized to the PL peak from the doped GaAs cap (not shown here). In (b), the QW peaks have been normalized to have the same intensities [13].

The PL energy shift of the InGaAs QW's was used to monitor the compositional disordering, while the linewidth and intensity of the PL emission was used to evaluate the relative number of nonradiative recombination sites left by the implantation and not removed by the annealing [23], [24]. Interpretation of linewidth and intensity are, of course, potentially complicated by changes in surface conditions and the creation of defects in the QW region.

Fig. 6 shows the PL peak from the InGaAs QW's obtained from as-grown samples together with spectra obtained after ion implantation and 30-s RTA. In the AlGaAs-based structure [Fig. 6(a)], the PL peak changes significantly as a function of ion implantation energy. For ion energies below 2 MeV (corresponding to an expected ion range $<1\ \mu\text{m}$, i.e., short of the QW structure) there is very little broadening and no shift of the QW peak. For implant energies between 2 and 4 MeV, for which the majority of defects are located in the vicinity of the active region, the PL peak is found to be very broad and weak (note the magnification factor in the figure), but does not shift upwards in energy. Above 4-MeV ion energy, corresponding to implantation of the ions beyond the QW, the peak exhibits an upward (blue) energy shift of about 30 meV and is again intense and quite narrow. This change occurs over a narrow range of implantation energies between 4 and 5 MeV. The energy shifts ΔE and peak widths are summarized in the top panels of Fig. 8.

A quite different picture is observed in the PL spectra from the InP-based material, shown in Fig. 6(b). The most obvious difference between these spectra and those of Fig. 6(a) is that substantial intermixing occurs already at very low implantation energies and shifts close to the maximum value are already obtained with ions having as little as 2-MeV energy, i.e., with projected ranges well short of the QW's. Furthermore, there is no energy region in which the linewidth is dramatically larger or the intensity significantly smaller than

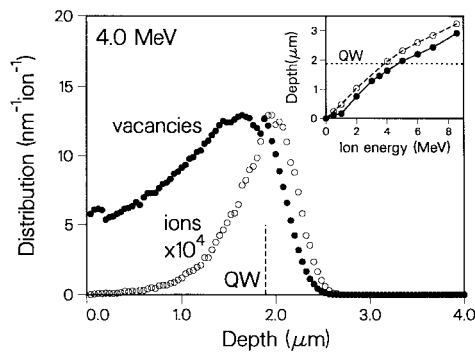


Fig. 7. Ion range (open circles) and vacancy (filled circles) distributions for 4-MeV arsenic implantation in the InGaAs–GaAs–AlGaAs structure, calculated using TRIM91 for ions incident at an angle of 7° to the surface normal. Note the discontinuities in the vacancy production at the depths corresponding to the cap and active region interfaces. The inset shows the depth corresponding to the peak in the implanted ion depth distribution and peak vacancy generation as a function of incident ion energy. The horizontal dotted line indicates the depth ($1.88 \mu\text{m}$) of the InGaAs QW [13].

at other energies. This implies that defect complexes in the QW region that might act as nonradiative recombination sites are either not created as easily in this InP-based system or are more efficiently removed during the anneal. In order to understand the different results obtained in these two-material systems, i.e., the importance of the initial distribution of ion-induced damage, TRIM 91 [25] simulations were used. Fig. 7 shows the results of such a simulation for both the implanted ion distribution and the total vacancy distribution (created by ions and recoils) for 4-MeV arsenic ions implanted into the InGaAs–GaAs–AlGaAs structure. The inset shows the depth at which the ion and total-vacancy distributions reach their maximum values as a function of implantation energy.

In the bottom panel of Fig. 8, the calculated concentrations of ions and vacancies created at the depth of the QW in the InGaAs–GaAs–AlGaAs structure are shown. In addition, the total number of vacancies created in the structure per incident ion is also displayed. There is a very good correlation between the energy at which the PL peak is most broadened (middle panel of Fig. 8) and reduced in intensity [Fig. 6(a)] and the energy at which the simulation predicts the peak in the ion distribution (end-of-range) to occur in the QW region. Furthermore, the magnitude of the blue shift after a 30-s anneal correlates well with the concentration of vacancies generated in the QW region, including a reduction in shift at the highest implant energy, where most vacancies are created significantly beyond the QW. The main point to be emphasized is that, after a 30-s anneal, intermixing occurs for the AlGaAs-based structure only at energies above 4 MeV, where the simulation predicts a sharp increase in vacancy creation at the QW.

Fig. 9 gives the same comparison of simulation and experiment for the InP-based structure. The damage produced per ion is lower in this case, mainly due to the lower scattering cross section and lower mass of the phosphorous ion relative to that of arsenic. The top panel shows clearly that, after a 30-s anneal, QWI occurs at energies for which no ions or vacancies have been deposited in the QW region. However, the correlation with the *total* number of vacancies created anywhere in the sample is very good. It can also be seen that the PL linewidth

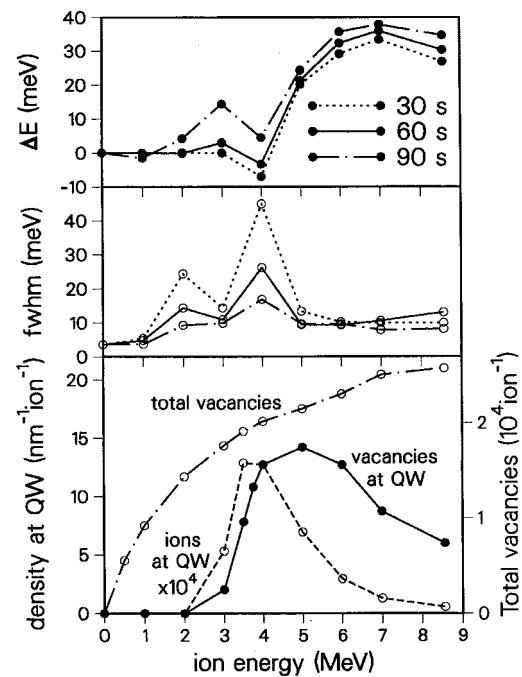


Fig. 8. PL and TRIM91 results for the InGaAs–GaAs–AlGaAs structure. Upper panel: energy shift ΔE in peak PL emission versus ion-implantation energy after 30-, 60-, and 90-s anneal at 850°C . Middle panel: corresponding FWHM of the PL peak. Lower panel: local implanted ion deposition and vacancy generation (number per nm per incident ion) at the depth of the QW ($1.88 \mu\text{m}$) and total number of created vacancies in the sample (number per incident ion) calculated with the TRIM91 program [13].

does not change as dramatically as in the previous sample and, for implantation energies up to 2 MeV, does not increase significantly from that observed in unimplanted material.

Considering first the InGaAs–GaAs–AlGaAs structure, the above data, together with earlier work [23], [24], [26] support the following picture of the intermixing process, which is assumed to be mediated by defects that must diffuse primarily through AlGaAs during the anneal. 1) Significant shifts in the PL peak energy, after the first anneal occur only at implantation energies for which the simulation predicts the creation of large numbers of vacancies in the QW region. Thus, for efficient QW intermixing by ion implantation to occur in InGaAs–GaAs QW's embedded in AlGaAs, the defects must be created in the vicinity of the QW. This suggests that the defect diffusion length in the $\text{Al}_{0.71}\text{Ga}_{0.29}\text{As}$ cladding layers is short during the RTA. This is in qualitative agreement with a very short neutral vacancy diffusion length ($\sim 0.1 \mu\text{m}$) found in a somewhat different $\text{Al}_{0.38}\text{Ga}_{0.62}\text{As}$ alloy [26]. Of course, there is a possibility that the defect diffusion is inhibited by the interface between the AlGaAs cladding and the GaAs barrier or is gettered in some fashion since there is a great deal of work reporting significant blue shifting in GaAs–AlGaAs QW's implanted with very low-energy ions. This issue requires further study [19]. 2) The maximum broadening and intensity reduction of the PL peak occurs at lower implantation energies than those resulting in large peak shifts and correlates well with the energy at which most of the implanted ions are deposited in the well region. It can be speculated that this is due to residual defect complexes acting as nonradiative recombination centers as previously reported

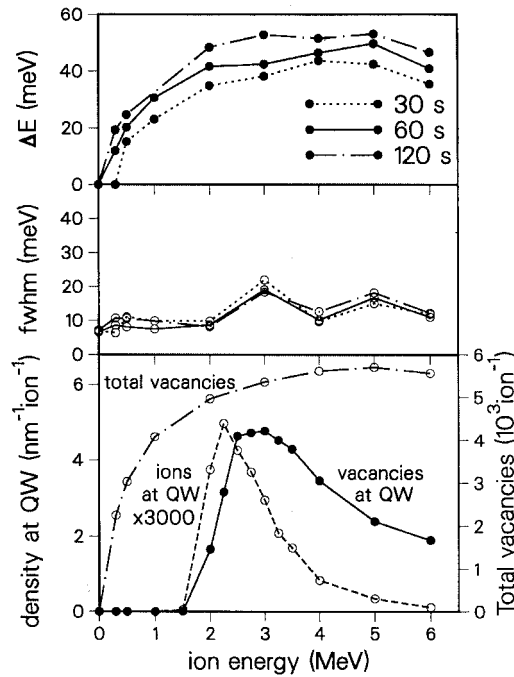


Fig. 9. PL and TRIM91 results for the InGaAs-InGaAsP-InP structure. Upper panel: energy shift ΔE in peak PL emission versus ion-implantation energy after 30-, 60-, and 120-s anneal at 700 °C. Middle panel: corresponding FWHM of the PL peak. Lower panel: local implanted ion deposition and vacancy generation (number per nanometer per incident ion) at the depth of the middle QW (1.83 μm) and total number of created vacancies in the sample (number per incident ion) calculated with the TRIM91 program [13].

[23], [24], [27], [28]. Such complexes may be hard to dissolve during annealing.

In the InGaAs-InGaAsP-InP structure, where defect diffusion occurs mostly through InP, the situation appears to be quite different. The strong correlation between the PL energy shift and the calculated *total* vacancy creation in the sample per incident ion suggests that the defects are extremely mobile in InP and that, wherever they are created in the structure, they can diffuse through the QW region and promote intermixing.

Figs. 8 and 9 also show the dependence of the peak shift and linewidth on annealing time for the two structures. In the case of the InGaAs-GaAs-AlGaAs structure (Fig. 8), the degree of intermixing increases slowly with anneal time suggesting the slow transport of defects to the QW region. This is particularly noticeable at 3 MeV, where vacancies are created just short of the QW's. At 4 MeV, intermixing is clearly retarded by more extensive damage. At energies for which ions are deposited in the QW region, the linewidth decreases with anneal time, confirming that the heavy QW damage is only slowly removed by the annealing process. For the InGaAs-InGaAsP-InP structure (Fig. 9), the situation is rather different. Following the 60-s or longer anneals, significant PL peak shifts are noticeable at *all* implantation energies, suggesting that defects can diffuse all the way from the cap region to the QW interfaces to promote intermixing.

The last two implant parameters to be reviewed in this section are the implantation temperature and dose rate dependence. The temperature dependence of ion-beam mixing in many materials is reasonably well understood in terms of standard treatments of radiation-enhanced diffusion. At low

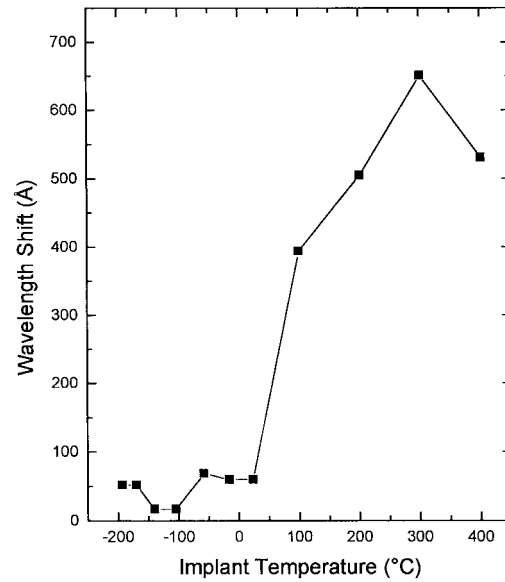


Fig. 10. PL wavelength shift in intermixed InP-based QW structure, plotted as a function of implant temperature. Data are displayed for a 1% compressively strained structure of similar composition to the one described in Fig. 4. The implantation conditions are: Dose = $1 \times 10^{15} \text{ P}^+/\text{cm}^2$ at 1 MeV; the ion flux was 120 nA/cm². The samples were then annealed by RTA at 675 °C for 90 s.

temperatures, mixing is mainly due to atomic transport within displacement cascades and is thus nearly independent of temperature. At higher temperatures, when point defects become mobile, the mixing increases exponentially with temperature.

Recently, the disordering of GaAs-AlGaAs and InGaAs-GaAs QW's by means of ion bombardment at elevated temperatures was reported [12], [29]. For both systems it was concluded that the effect of implanting at high temperatures is to enhance the diffusion and recombination of interstitials and vacancies. The net result of high-temperature implantation is a steady-state interstitial-vacancy population, which enhances the mixing of the QW with a minimum of residual damage left after implantation and RTA.

Another study has demonstrated the effect of varying the sample temperature during irradiation upon the magnitude of intermixing of InP-based laser diode structures [30]. For otherwise identical processing conditions, they show that varying the irradiation temperature of the InP-based laser structure has little effect below room temperature but acts to greatly enhance the magnitude of the induced blue shift above it. These results are summarized in Fig. 10 for a 1% compressively strained structure, similar to the structure illustrated in Fig. 4. It was concluded that, as the implanted ions come to rest at shallower depths than the QW's, the defects responsible for enhancing intermixing must diffuse significant distances to reach the active region. Since large diffusion lengths are inferred for these defects in InP-based materials, it is most likely that changes in the residual implant damage are controlling the response of the bandgap energy to implant temperature. Indeed, for the irradiation of InP under conditions similar to the present study, a critical regime exists between room temperature and 100 °C in which damage levels decrease from saturation to a very low level across a temperature interval of only 10 °C [31]. This

behavior in other semiconductor systems has been described in terms of a competition between dynamic defect annealing and production rates, influenced by a combination of implant parameters [32]. Finally, dose rate effects on amorphization or on interdiffusion are generally thought to be the result of both temporal and spatial overlap of defects within the collision cascades. Studies on dose rate effects on damage accumulation in implanted III–V materials have shown that the generation rate of interstitial-vacancy pairs increases with increasing ion flux (dose rate) [33]. It has recently been shown [12] that the intermixing of heterostructures is also dose rate dependent. The explanation of this phenomenon is most likely similar to the one proposed for the amorphization of bulk III–V materials [34].

B. Waveguiding Characteristics

As mentioned in the introduction, the practicability of monolithic integration of components in III–V semiconducting structures depends critically on a simple, inexpensive technique for fabricating devices of different functionalities on a single wafer. These devices have to be integrated and coupled optically to each other, requiring the need of low loss waveguiding elements. In fact, the optical characteristics of waveguides in the integration process are presumably the most important features to be maintained and optimized (e.g., low residual absorption) for any integration technique to be viable. The research group at NRC was the first to measure the waveguide characteristics of high energy ion-induced QWI in InP-based laser structures [35].

The sample studied was an unstrained laser structure containing five $\text{In}_{0.53}\text{Ga}_{0.47}\text{As}$ QW's with $\text{In}_{0.74}\text{Ga}_{26}\text{As}_{0.57}\text{P}_{0.43}$ barriers and is the one represented in Fig. 4 (right panel). Ion implantation was performed using phosphorous ions to avoid doping the structure. A constant flux of 6.6 nA/cm^2 was used to implant a dose of $2.5 \times 10^{13} \text{ ions/cm}^2$ with an energy of 2 MeV, at a substrate temperature of 200 °C. During implantation, the sample was tilted 7° to the surface normal to minimize ion channelling. The expected mean range of the ions (according to the simulation program TRIM 91 [25]) was 1.5 μm , i.e., well short of the active region of the laser structure which is $\sim 2 \mu\text{m}$ underneath the surface. The study above showed that, in the InGaAsP–InP system, the degree of intermixing (PL blue shift) correlates with the total number of vacancies created in the sample rather than the vacancies created locally in the QW's, since defects are extremely mobile in InP [13]. After implantation, the structure was annealed in a N_2 atmosphere using an AG Associates 410 Rapid Thermal Annealer at a temperature of 700 °C for 120 s. The sample surface was protected from desorption during annealing by placing a large piece of GaAs face down upon it and using GaAs substrate material along side the four sample edges to minimize thermal nonuniformity during the RTA process. Low-temperature PL measurements complemented by room temperature PL mapping were used to verify the bandgap shift, uniformity and optimization of the processing conditions [13]. With the exception of a 300- μm strip along the sample edges, PL intensity and uniformity were excellent.

In order to investigate the effect of ion implantation on waveguide quality, waveguide loss measurements using the

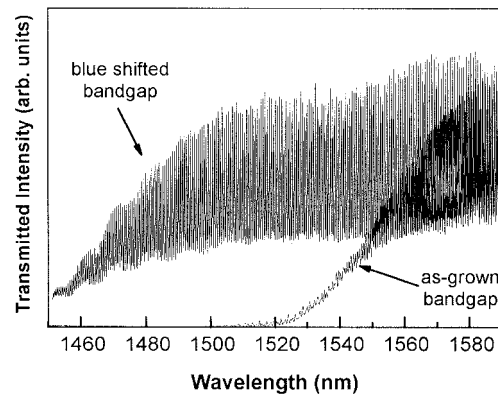


Fig. 11. Measured transmission spectra of implanted (blue-shifted bandgap) and unimplanted (as-grown bandgap) QW waveguides.

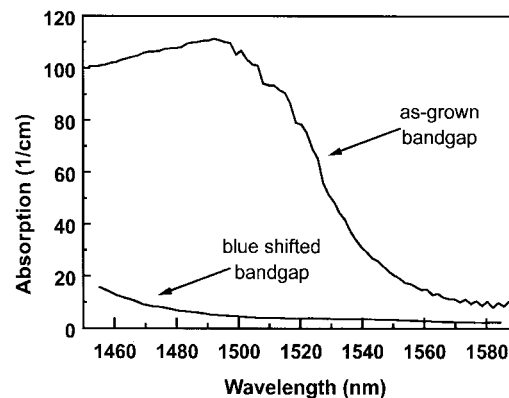


Fig. 12. Absorption constants derived from measured transmission spectra using modulation ratio and average transmission intensity for both as-grown and blue-shifted waveguides.

Fabry–Perot fringe technique were performed. 4- μm -wide ridge waveguides were fabricated both on the intermixed region and on the nonmixed region. The sample was then cleaved to form a 1-mm-long Fabry–Perot cavity. A tunable (1.45–1.59 μm) laser diode was used for the absorption experiments. The light was modulated at 10 kHz and coupled into the TE mode of the waveguide through a tapered polarization preserving fiber. The transmitted light was then captured by a similar fiber coupled to a Ge-detector followed by a lock-in amplifier.

Fig. 11 shows the measured transmission spectra of the implanted and unimplanted waveguide cavities. Fabry–Perot interference fringes were formed due to multiple reflections at the cleaved facets. From the contrast of these fringes the waveguide loss can be determined [36]. A change in the refractive index, between the unimplanted and implanted waveguides, can also be extracted from the spacing of the fringes and yields a value of $\Delta n = 0.08$ ($\sim 2.5\%$) at 1550 nm. It should be noted that, for photon energies larger than the bandgap, the Fabry–Perot fringes disappear due to the high absorption, and therefore another method based on the relative transmitted intensity was used.

Fig. 12 presents the absorption as a function of wavelength derived from the measured transmission spectra using both methods for the implanted and the unimplanted waveguides. As observed from the spectra, the bandgap of the implanted QW's was blue-shifted 90 nm with respect to the as-grown

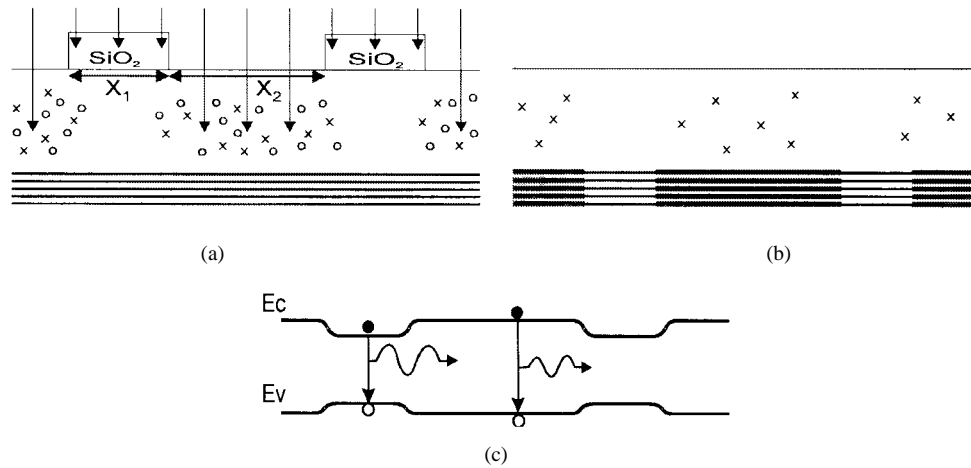


Fig. 13. Schematic cross section through sample illustrating selective area intermixing of five QW's located $1.77 \mu\text{m}$ below the surface. (a) Ion implantation of P^+ ions using a patterned $2.0\text{-}\mu\text{m}$ -thick silicon dioxide mask. (b) After rapid thermal annealing, QW's underneath implanted regions and near the edges of masked regions have been intermixed. (c) Resultant change in the bandgap energy of the QW's along the lateral direction.

QW's. The actual bandgap cannot be observed since it is beyond the range of the tunable source. At the absorption edge of the unimplanted waveguide ($\sim 1.54 \mu\text{m}$), the absorption coefficient is reduced from 110 cm^{-1} to only 4 cm^{-1} . Note that this absorption value also includes excess losses such as scattering losses resulting from imperfections of the ridge waveguide. It should be noted that the loss in the implanted waveguide appears to be lower than the unimplanted one, even after considering the 90-nm difference in bandgap. For example, the absorption of the unimplanted waveguide is $\sim 8 \text{ cm}^{-1}$ at 1580 nm , while it is 5 cm^{-1} at 1490 nm for the implanted sample. This indicates that no excess loss results from the damage created by the implantation. This decrease could be due to a reduction in Auger effects and intervalence band absorption, as the bandgap wavelength becomes shorter [37]. In addition, the free carrier absorption coefficient is, to a first approximation, proportional to the square of the wavelength and so would be reduced by about 12% over the range of wavelength studied. Another contributing factor is that the guided mode will be more strongly confined within the active region as the wavelength is reduced, decreasing the interaction of the mode with doped regions in the cladding layers.

The successful demonstration of high energy ion implantation for blue-shifting the bandgap of InGaAs-InGaAsP QW waveguide structures by 90 nm (in an all-planar process), and reducing the absorption from 110 to 4 cm^{-1} at the original lasing frequency, is a good indication of the viability of this technique for integration purposes. It is also worth noting that the effective index of the waveguide in the transparent region, beyond the bandgap energy, is reduced by about a percent or two in the intermixed QW waveguide compared with the as-grown QW waveguide. This is a very large change in effective index (as much as an order of magnitude larger than that produced by fabricating ridges) and can be utilized to design unique QW waveguide devices, such as buried waveguides.

However, in order to design and fabricate such structures, the lateral selectivity of the ion-induced QWI technique has to be established. The use of PL and a specially designed mask to

monitor the intermixing of QW's under masked regions were employed to address this issue [38]. The structure used in this study is again the same as the one represented in Fig. 4 (right panel). The implantation conditions were, again, such that no P^+ ions reach the active region of the structure (i.e., Dose $= 1.0 \times 10^{14} \text{ cm}^{-2}$, Energy $= 1.0 \text{ MeV}$, Flux $= 7 \text{ nA/cm}^2$, $T_{\text{substrate}} = 200 \text{ }^\circ\text{C}$). Prior to implantation, a $2.0\text{-}\mu\text{m}$ silicon dioxide layer was deposited on the surface and patterned to act as a selective area mask (the mask pattern is described in more detail below). Where it covered the surface, the thick oxide completely blocked any ions from reaching the sample.

After implantation, the silicon dioxide was removed and the samples were rapid thermal annealed at $675 \text{ }^\circ\text{C}$ for 180 s in flowing nitrogen. GaAs pieces were used to surround and cover the sample in order to reduce desorption of As from the surfaces. These conditions were previously found to give a near-zero shift in the PL peak of as-grown material, while energy shifts of implanted material were saturated.

The implantation mask had 13 distinct arrays, each containing parallel stripes of oxide of nominally the same width and spacing [X_1 and X_2 respectively, as shown in Fig. 13(a)]. From one array to the next, the mask stripe width X_1 varied from 1.5 to $23.5 \mu\text{m}$, while the spacing between masked stripes X_2 also increased proportionately from $6.5 \mu\text{m}$ to $32.5 \mu\text{m}$ (the regions between masked stripes will be referred to as implanted stripes). Each array was approximately 1.2 mm square, and thus contained twenty or more masked stripes. During low-temperature (5 K) PL, the excitation laser was directed at the center of an array, with a spot size of approximately $100 \mu\text{m}$. Due to this spot size, the PL spectra from an array exhibited luminescence peaks from both the implanted and the masked regions. The excitation laser was a Ti:Sapphire tuned to 880 nm with an excitation power of a few milliwatts.

Low-temperature PL spectra of these samples are shown in Fig. 14. Spectra A and B are reference spectra taken from relatively large regions of the same material which were completely masked and implanted, respectively, while spectra C through G were taken from arrays with masked stripes of varying widths (X_1). Spectra from arrays which are not shown

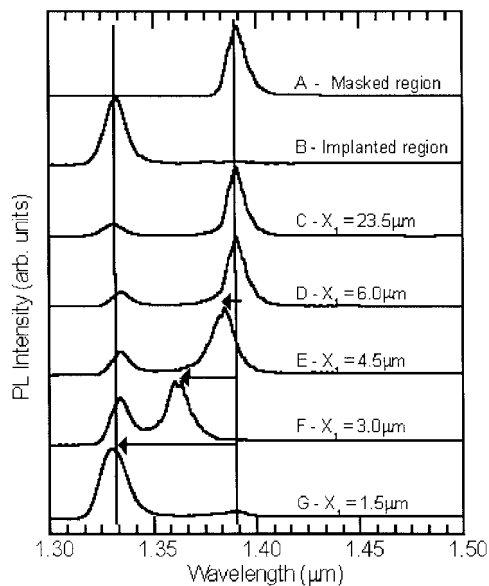


Fig. 14. Normalized low-temperature (5 K) PL spectra from a large masked region (spectrum A), a large uniformly implanted region (spectrum B), and from arrays with varying mask stripe widths, as noted by the value of X_1 (spectra C through G).

(those from arrays with X_1 between $6.0 \mu\text{m}$ and $23.5 \mu\text{m}$) were nominally identical to spectra C and D. For spectra C through G, the longer wavelength peak at $1.39 \mu\text{m}$ is taken to be from the QW's underneath masked stripes (i.e., unaltered), while the shorter wavelength peak at $1.33 \mu\text{m}$ originates from intermixed QW's (i.e., in the implanted regions). For $X_1 \geq 6.0 \mu\text{m}$, the PL peak from masked stripes is in the same position as peaks from the reference spectra A, but as masked stripes become narrower (spectra E and F) these peaks are blue shifted due to partial intermixing of the QW's. The degree of intermixing increases until this peak merges with $1.33 \mu\text{m}$ peak of the neighboring implanted stripes (spectra G). In contrast, implanted stripes from all arrays were blue shifted by approximately the same amount, 57 nm (40 meV), equal to the shift of uniformly implanted material (spectra B). PL linewidths of unaltered QW's were $8 \pm 1 \text{ nm}$ ($6 \pm 1 \text{ meV}$), and those of intermixed QW's were slightly larger at $10 \pm 1 \text{ nm}$ ($8 \pm 1 \text{ meV}$). Linewidths of partially intermixed "masked" stripes (of spectra F and G) were comparable to those of the implanted stripes.

If the positions of PL peaks from both implanted and masked stripes are compared with the peak position of masked regions from surrounding material, an energy shift can be obtained. The mask stripe width, X_1 , is divided by 2 to give a value for the lateral distance from a mask edge. In Fig. 15, a plot showing the energy shift as a function of $X_1/2$ clearly indicates that QW's within the first $2.5 \mu\text{m}$ of a mask edge undergo some degree of intermixing. From these observations, the lateral selectivity of QWI on these structures with this implantation energy is determined to be $2.5 \mu\text{m}$.

The intermixing of QW's under masked regions will be due to two effects: 1) the lateral spread of ions during implantation, and thus the lateral distribution of point defects to regions under the mask edge and 2) the lateral diffusion of defects

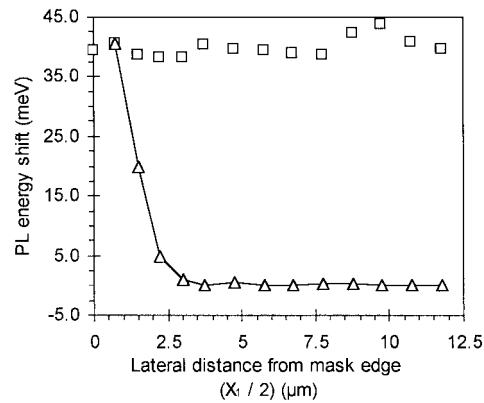


Fig. 15. Energy shifts of PL peaks from QW's in implanted stripes (squares) and masked stripes (triangles). The shift is obtained by comparison to PL peaks in fully masked regions surrounding each array.

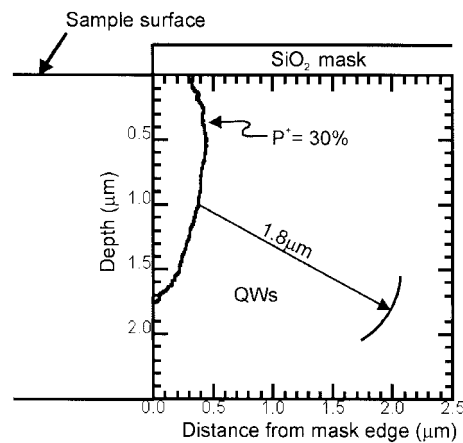


Fig. 16. The lateral straggle of implanted ions to regions under the mask edge, shown as a function of depth into the sample. The plot shows an isoconcentration contour where P^+ ion concentration drops to 30% of its uniform implantation concentration. Superimposed on the plot is a wavefront with radius of $1.8 \mu\text{m}$, depicting a possible path for the diffusion of defects created by the straggling ions.

during annealing. Here, we do some very rough calculations to demonstrate the approximate magnitudes of these two effects. Using SRIM97 [39]² to simulate the implantation, a plot of the lateral straggle of ions as a function of depth, as shown in Fig. 16, was obtained (this gives the distance at which the ion concentration drops to approximately 30% of its uniform implantation value). As was discussed in Section III-A, all defects, including those created near the surface, are able to diffuse to QW's and cause intermixing [13], thus diffusion lengths of defects can be taken to be at least $1.8 \mu\text{m}$. A wavefront with a radius of $1.8 \mu\text{m}$ is added to the plot of Fig. 16, illustrating a path (with the largest lateral reach) for the diffusing defects created by straggling ions. This wavefront of diffusing defects is able to reach the regions of the QW's that are at a lateral distance of $2.0 \mu\text{m}$ from the mask edge. Thus QW's at this position will exhibit a small amount of intermixing, while regions slightly further under the mask will not be intermixed at all. This rough

²The latest version of TRansport of Ions in Matter (TRIM) is called SRIM'97 (Stopping Range of Ions in Matter); for a theoretical basis, see [39].

prediction agrees well with the experimental results of Fig. 15. In reality, the effects of ion straggle and lateral diffusion cannot simply be summed; a more accurate prediction would require numerical modeling taking into account the damage distribution caused by straggling ions and proper diffusion equations. It may be possible to experimentally determine with more precision the roles of the two processes (ion straggle and lateral diffusion) through repetition of this experiment with other implant energies.

As previously indicated, the blue shift of the energy bandgap, which results from the intermixing process, also induces a decrease in the refractive index of the QW's at energies below the bandgap [35]. This property has been used to create devices with lateral optical confinement, including waveguides, index-guided lasers, and modulators in GaAs-AlGaAs [40] and waveguides in InGaAs(P)-InP [41]. In a recent paper, buried waveguides (BWG's) were fabricated in an InGaAs-InGaAsP laser structure using QWI, and the refractive index change Δn evaluated [42]. Here, again, high energy ion implantation of nonimpurity species (phosphorus) was used to intermix the QW structure. This technique has potential for the fabrication of index-guided buried-heterostructure lasers.

The sample used in this study was the InGaAs-InGaAsP structure of Fig. 4 with the uppermost QW situated $1.77 \mu\text{m}$ below the surface. It was implanted with 1.0-MeV phosphorus ions to a dose of $1.0 \times 10^{14} \text{ cm}^{-2}$ and annealed at 675°C for 180 s [38]. A patterned SiO_2 layer was used to mask selected areas during implantation, then removed before annealing. A blue shift of 60 nm was observed between the photoluminescence peaks of implanted and masked regions. The latter PL peak was identical to that seen in as-grown material.

The BWG's of this study consist of a narrow stripe of as-grown material, defined by an SiO_2 implantation mask stripe, surrounded by implanted and intermixed regions. The difference in refractive index between as-grown and intermixed material results in lateral optical confinement along the stripe. Large implanted and masked areas, located elsewhere on the sample, were used to make slab waveguide (SWG) measurements of as-grown and intermixed material. The sample was cleaved to form a 1.0-mm -long Fabry-Perot cavity. Measurements were performed using a tunable ($1.45\text{--}1.59 \mu\text{m}$) diode laser, modulated at 10 kHz , and detected using a Ge detector and lock-in amplifier. Polarization-preserving fibers were used to couple light into the waveguides and to collect transmitted light; lenses at the fiber ends focused to a spot size of approximately $2 \mu\text{m}$.

Fig. 17 shows the transmission spectra (which have been smoothed and normalized) for four different waveguides: intermixed and as-grown SWG's, and BWG's formed using 6.0 and $4.5 \mu\text{m}$ SiO_2 implantation mask stripes. There are three important characteristics of the transmission spectra. First, due to limits in the lateral selectivity discussed above, partial intermixing under mask stripes results in a small blue shift of the BWG's bandedge from the as-grown bandedge. In fact, BWG's fabricated with narrower stripes widths were completely intermixed, and thus behaved much like the intermixed SWG's. Second, at longer wavelengths, the

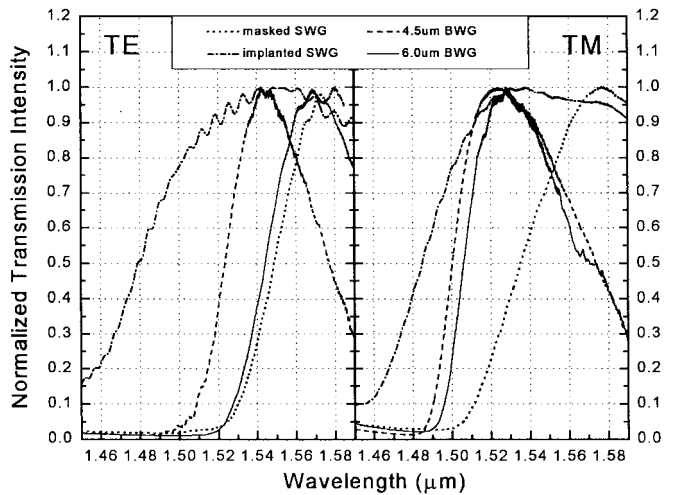


Fig. 17. Normalized and smoothed transmission intensity as a function of wavelength for as-grown and intermixed SWG's, and for 4.5- and $6.0\text{-}\mu\text{m}$ -wide BWG's.

transmission intensities of the BWG's decrease at a much faster rate than for the SWG's, indicative of a decrease in the BWG's ability to guide the light. Third, the bandedges of the TE and TM modes for the as-grown SWG do not coincide, as is expected for a QW structure, but they do coincide (to within $2\text{--}3 \text{ nm}$) in the case of the intermixed SWG. We attribute this to a buildup of strain in the intermixed QW's due to higher diffusion rates on the group V sublattice over the group-III sublattice. This will be discussed in greater detail later. The increased strain shifts the heavy-hole (HH) and light-hole (LH) bands such that they overlap. Thus, the 4.5- and $6.0\text{-}\mu\text{m}$ BWG's exhibit a reduced birefringence in comparison to the as-grown SWG. We postulate that with a larger degree of intermixing, such that in the intermixed material forming the "lateral cladding" the TE bandedge is at a shorter wavelength than the TM bandedge, it may be possible to achieve a polarization insensitive buried heterostructure.

The transmission spectra shown in Fig. 17 have been smoothed for clarity, thus removing the high-frequency Fabry-Perot interference fringes formed owing to multiple reflections at the cleaved facets. The intensity contrast of these Fabry-Perot fringes was used to calculate absorption losses [36]. For TE polarization and the $6.0\text{-}\mu\text{m}$ BWG, the losses were found to be 180 dB/cm at $\lambda = 1.52 \mu\text{m}$ (the lasing wavelength of original material) decreasing to 40 dB/cm at $\lambda = 1.56 \mu\text{m}$. For the $4.5\text{-}\mu\text{m}$ BWG, the losses were lower: 75 dB/cm at $\lambda = 1.52 \mu\text{m}$ and 30 dB/cm at $\lambda = 1.55 \mu\text{m}$. The lower values for the $4.5\text{-}\mu\text{m}$ BWG are expected as the bandedge is slightly shifted from that of the as-grown QW's. Here, again, a larger degree of intermixing and/or a purposeful, but small amount of intermixing at the waveguide center could be advantageous for reduced absorption losses at the as-grown wavelength.

The refractive index is calculated from the frequency of the Fabry-Perot fringes [36] and results are presented in Fig. 18. The decrease in refractive index due to QWI can be taken as the difference between the as-grown and intermixed

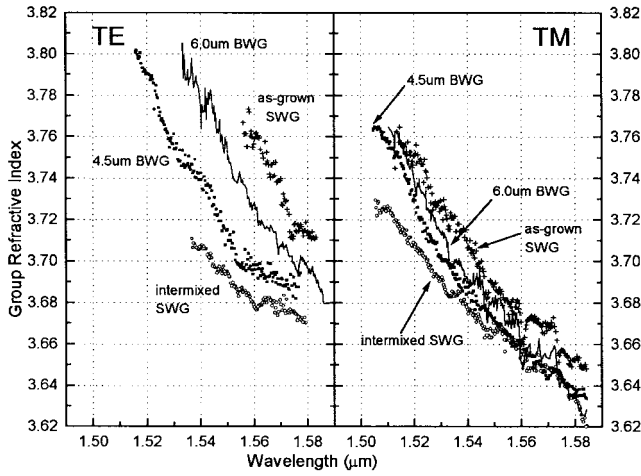
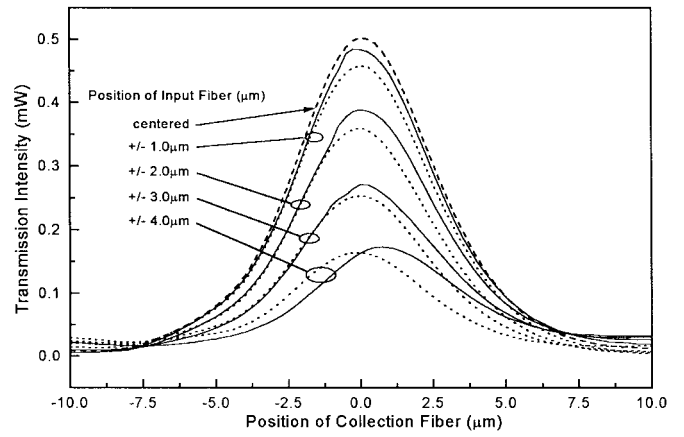


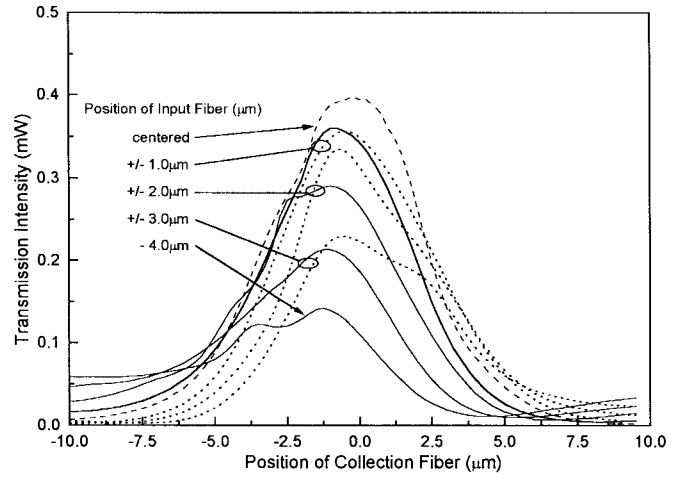
Fig. 18. The refractive index as a function of wavelength, as calculated from the frequency of the Fabry-Perot fringes in transmission measurements, for as-grown and intermixed SWG's, and for 4.5- and 6.0- μm -wide BWG's.

SWG's measurements. This difference decreases at longer wavelengths, which will result in weaker guiding, as is evident in the transmission spectra (Fig. 17). Between 1.58- and 1.54- μm Δn is 1.2%–2.8% for TE, and 0.6%–0.9% for TM. These values increase at shorter wavelengths, but increased absorption precludes accurate measurements. The effective refractive index of BWG structures lie in between the as-grown and intermixed SWG refractive indexes, as expected.

To evaluate the modal behavior of the guided modes, near-field scans of the output beam were taken for different positions of the input beam. By varying the horizontal position of the input fiber, higher order modes can be excited, and if supported by the waveguide, will be present in its output profile. Fig. 19(a) gives an example of such a study on the 4.5- μm BWG at $\lambda = 1.54 \mu\text{m}$ (TE), and shows that the waveguide is truly single mode at these conditions (the very small horizontal shift of the output profile at substantially off-centered input positions is attributed to the contributions of low-intensity slab modes). When repeated for different wavelengths, the 4.5- μm BWG showed single-mode guiding for all wavelengths $\lambda = 1.52$ to $1.59 \mu\text{m}$ for both TE and TM polarizations (again, profiles for shorter wavelengths are not easily evaluated due to high absorption losses). In comparison, the near-field profiles for the 6.0- μm BWG indicate multimode behavior for wavelengths lower than $1.57 \mu\text{m}$, and single-mode behavior above it, for both TE and TM modes. Fig. 19(b) is an example of the multimode behavior for the 6.0- μm BWG at $\lambda = 1.56 \mu\text{m}$ (TE). We expect the multimode behavior of the 6.0- μm BWG to be due to both its larger width and larger effective refractive index (at a given wavelength) in comparison to the 4.5- μm BWG. In summary, the spatially selective nature of ion-induced QWI permits the fabrication of narrow, index-guiding buried heterostructures, where refractive index differences are of the order one or two percent. In the work presented here, devices exhibited both single-mode and multimode guiding, depending on the wavelength and guide width. A lower degree of intermixing will result in less confinement and therefore increase the window for single mode guiding. Alternately, a higher degree of intermixing



(a)



(b)

Fig. 19. Near-field profiles of the BWG structures obtained by horizontally scanning the collection fiber at the waveguide's output for a given position of the input fiber, and then repeating for different positions of the latter. (a) Single-mode behavior is evident for the 4.5- μm BWG at a wavelength of $1.54 \mu\text{m}$ (TE). (b) Multimode behavior of the 6.0- μm BWG at $1.56 \mu\text{m}$ (TE).

could reduce the birefringence and the absorption losses at the expense of multimode behavior. More analysis and modeling of these structures will be presented later.

C. Electrical Characteristics

For the ion-induced QWI process to be a useful technique for lateral bandgap control in monolithic integration, it is essential that the electrical characteristics of the p-i-n structure not be degraded by the implantation and/or anneal. Fig. 20 shows the current versus voltage (I - V) characteristics for the as-grown and implanted materials following a 90-s RTA at 700°C [35]. We see that all samples have very similar I - V characteristics. The implanted samples show a slightly higher reverse leakage, which is negligible from the point of view of device operation. Finally, for all the diodes made from the nonimplanted and implanted samples, no breakdown occurred for reverse-biases up to 15 V.

Another key requirement for monolithic PIC's fabricated using this technique is that the electrical properties of active devices with intermixed QW's be comparable to those of as-

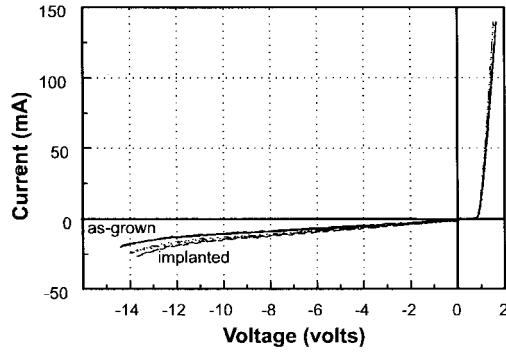


Fig. 20. I - V characteristics of p-i-n diodes made from as-grown and implanted material.

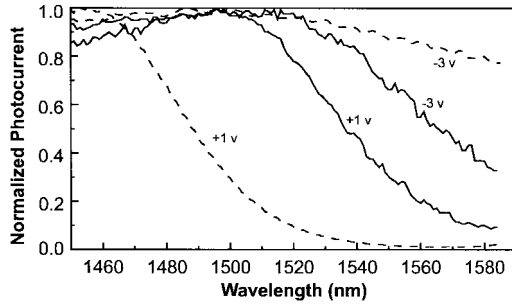


Fig. 21. Quantum-confined Stark effect in as-grown (solid lines) and QWI (dashed lines) waveguides. Only the effects of two voltages (+1 V cancels the built-in electric field and produces near zero internal electric field and -3 V corresponds to an inverse electric field of about 110 kV/cm) are shown.

grown QW's. To study this requirement, both forward (diode laser) and reversed biased (electroabsorptive modulator and detector) QW intermixed laser structures were investigated. This will be described in detail in the next section.

IV. APPLICATIONS OF QWI IN ACTIVE DEVICES

A. Electroabsorptive Modulator

With increasing reverse electrical bias, the bandgap energy of the QW shifts to longer wavelength due to the quantum confined Stark effect, as illustrated in Fig. 21 for both as-grown (solid lines) and intermixed QW's (dashed lines) [15]. Intermixing increases the bandgap energy (shifts it to shorter wavelengths) but, in both cases, increasing external reverse voltage shifts the bandedge to lower energies (longer wavelengths). The magnitude of the shift for a given bias is significantly increased due to the rounding of the shape of the QW, which permits a given electric field to move electrons and holes further apart.

B. Bandgap Tuning of InP-Based Lasers

Intermixing of MQW's can also be used to shift the gain envelope of as-grown material to allow lasers with a range of wavelengths to be fabricated from a single wafer. This is particularly relevant to WDM systems [17]. For example, the InP-based 1.5- μm laser structure of Fig. 4 was implanted with phosphorous ions to a dose of $2.5 \times 10^{13} \text{ P}^+/\text{cm}^2$ at an energy of 1 MeV. The implant was performed at a temperature

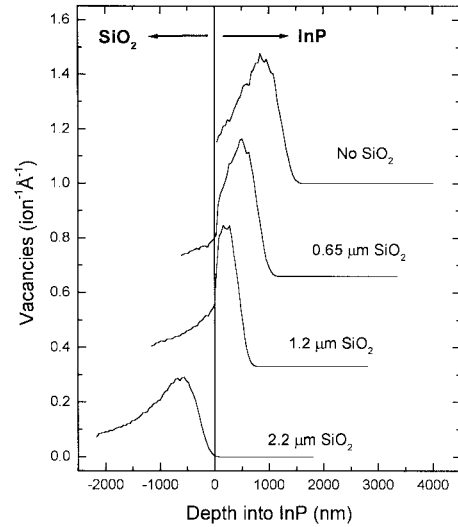


Fig. 22. Vacancy distributions for 1-MeV phosphorus implantation in the InP-based laser structure for different SiO_2 mask thicknesses (2.2, 1.2, 0.65, and 0 μm) evaporated on top of the structure. The calculation was done using the TRIM-91 code for an incident angle of 7° . (0 denotes the interface between the SiO_2 mask and the laser structure).

of 200 $^\circ\text{C}$ and a flux of $6.6 \text{ nA}/\text{cm}^2$ [43]. Here again, the energy of the ions was chosen so that the expected range was well short of the active region of the laser structure, which is $\sim 2 \mu\text{m}$ underneath the surface. The expected mean range of the ions, according to the simulation program TRIM 91 [25], was 0.88 μm . After implantation (and after removal of the mask, see below) the structure was annealed under the usual conditions.

As was previously discussed in Section III-A, for InGaAs-InGaAsP QW's embedded in InP cladding layers, a strong correlation exists between the PL energy shift after implantation and annealing and the calculated *total* vacancy creation in the sample per implanted ion [13]. This observation suggests that defects are extremely mobile in InP and that, wherever they are created in the structure, they can diffuse through the QW region and promote intermixing. Therefore, an increase in either dose or energy of the implanted ions will lead to an increase in intermixing. For simplicity, we decided to keep the dose and energy of the ions fixed and vary the damage generated in the semiconductor structure by masking different parts of the sample with different thicknesses of SiO_2 , obtained through standard UV lithography and SiO_2 PECVD evaporation. Three different SiO_2 layer thicknesses, 0.65, 1.2, 2.2, and μm , and an unmasked region, i.e., 0 μm , were deposited on a single piece of laser material. The maximum SiO_2 thickness was chosen so that the 1-MeV P^+ ions would be completely stopped in the SiO_2 , leaving unimplanted material beneath. Fig. 22 shows the calculated vacancy distributions for the 1-MeV P^+ implant in the laser structure covered with the different SiO_2 layer thicknesses. The SiO_2 layers were again removed before thermal treatment (RTA).

Low-temperature (5 K) PL measurements were made using weak (1-mW) titanium-sapphire excitation tuned below the InP bandgap. The diameter of the exciting beam was 100 μm .

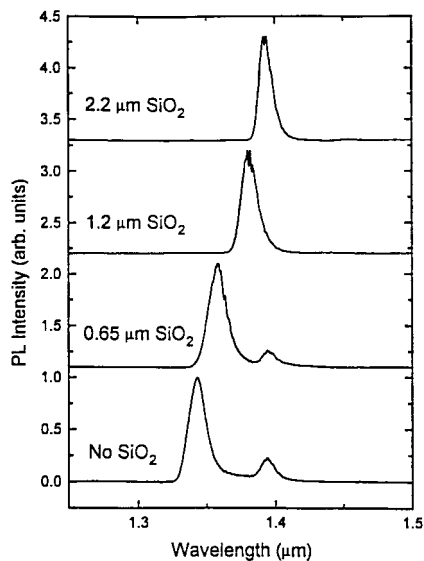


Fig. 23. Low-temperature (5 K) PL spectra obtained from the laser structure which was masked, implanted and annealed. The implantation used 1-MeV ions at a dose of $2.5 \times 10^{13} \text{ P}^+/\text{cm}^2$, at an implant temperature of 200 °C, 7° to the surface normal. The RTA was performed at 700 °C for 90 s. The PL peak positions are 1.3434, 1.3581, 1.3816, and 1.3957 μm .

The low-temperature PL spectra obtained from the four implanted and annealed regions of such a laser structure are shown in Fig. 23 [43]. Reproducible results were obtained from other pieces of the same sample. As expected, the magnitude of the blue shift in the PL emission correlates with the total number of defects generated in the laser structure [13]. Where the SiO_2 mask was the thickest, no disordering took place and the peak of the PL emission is at 1.396 μm (1.56 μm at room temperature). In the case where no SiO_2 mask was used, maximum interdiffusion was achieved and the PL emission was blue shifted by 52 nm. The weaker emission band observed at 1.396 μm from implanted regions which have 0.65- μm SiO_2 and no SiO_2 can be attributed to the laser spot size extending over nonintermixed areas of the sample. The PL linewidth does not increase significantly (FWHM increases from 10 to 13 nm) as the intermixing increases. This small change could be due to variation in the degree of intermixing across the probed area. Finally, the integrated PL intensity, which is strongly influenced by nonradiative recombination sites left by the implantation and not removed by the anneal, does not decrease with increased disordering. This demonstrates that the crystalline quality of the device can be maintained after interdiffusion.

Broad area lasers were fabricated from this material and tested at room temperature under pulsed conditions (1- μs pulses at a repetition rate of 1 kHz). Fig. 24 shows the lasing spectra from the four regions, fabricated from the same sample, which have undergone different degrees of intermixing (blue shifted as much as 63 nm). Furthermore, the threshold current measured from lasers fabricated from material with different degrees of intermixing was essentially constant, ~ 410 mA (see Fig. 24, caption). This is the same value obtained from laser structures fabricated from the as-grown wafer and indicates the high quality of the blue-shifted laser material,

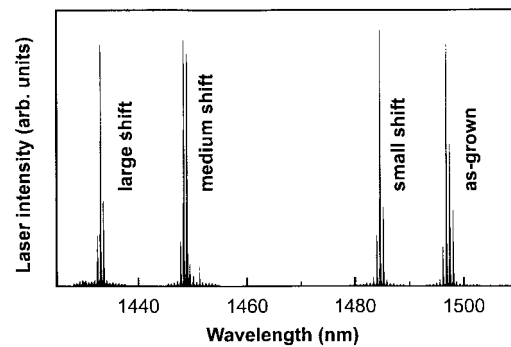


Fig. 24. Emission spectra of the bandgap-shifted broad-area lasers ($60 \mu\text{m} \times 500 \mu\text{m}$). The emission wavelength, external quantum efficiency, and threshold current are: (a) 1497 nm, 30.7%, 410 mA; (b) 1485 nm, 31.5%, 410 mA; (c) 1449 nm, 25.8%, 400 mA; (d) 1433 nm, 24.6%, 420 mA; for SiO_2 mask thicknesses of 2.2, 1.2, 0.65, and 0 μm , respectively.

as any damage left in the active region of the device after implantation/anneal would add to the loss in the cavity and increase the threshold current. This observation suggests that factors contributing to changes in the threshold current such as alteration of the well shape, intermixing and dopant diffusion in the graded index structure and changes in the number of nonradiative recombination centers within the material are not significant. The external quantum efficiency was also determined and showed to decrease slightly from 30.7% to 24.6%, with intermixing (see Fig. 24, caption). This decrease probably originates from the modification of the QW/barrier potential difference, which decreases after intermixing has taken place, as evidenced by the PL blue shift [44]. This change would allow the thermionic emission of the electrically injected carriers to increase.

C. Laser Diode Reliability After Intermixing

Although it is clear from the studies discussed above that QW shape modification produces no short term deleterious effects on the optical and electrical properties of active device structures, residual damage may produce cumulative effects and eventually reveal itself during the operation of these devices by, for example, reducing lifetimes. In order to study this possibility, accelerated lifetime tests were performed on a series of QW intermixed laser diodes [45]. These were stressed by operating them with large forward currents and at elevated temperatures.

High-energy phosphorous ion implantation was used to selectively control the bandgap energy of InGaAsP-InP QW laser structures operating at 1.31 μm . Since P is a lattice constituent, the implant introduces no additional material doping if it occupies a column V site. One should keep in mind, however, that the excess P being added to the crystal along with damage could result in some concentration of antisite and interstitial defects being produced and hence act as donor or acceptor species. More importantly, no active impurities (dopants) were introduced into the host material from the implantation process. This is important in waveguide PIC's where high electrical resistivity between active devices must be maintained and free-carrier absorption loss should be minimized.

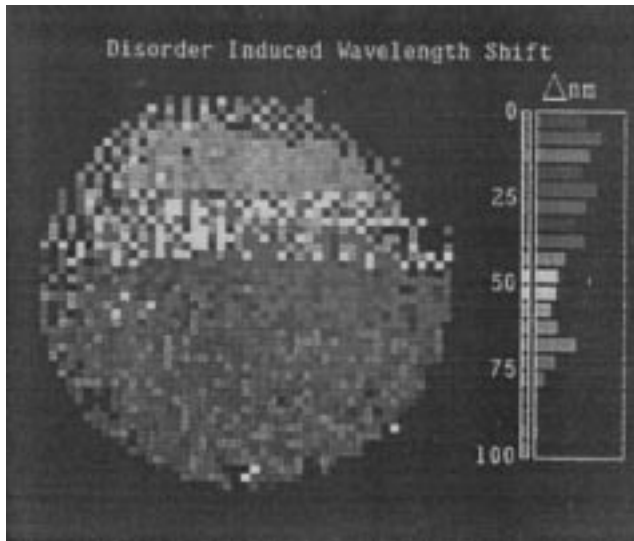


Fig. 25. Ion-induced QW disordering PL map obtained at room temperature on a processed 50-mm wafer InGaAsP-InP QW laser structure. The four regions represented correspond to the following. Region 1: Lower part of the wafer, $1.6\text{ }\mu\text{m SiO}_2$, $\lambda\Delta \sim 0\text{ nm}$. Region 2: Lower-middle part of the wafer, $1.1\text{ }\mu\text{m SiO}_2$, $\lambda\Delta \sim 30\text{ nm}$. Region 3: Upper-middle part of the wafer, $0.7\text{-}\mu\text{m SiO}_2$, $\lambda\Delta \sim 45\text{ nm}$. Region 4: upper part of the wafer, $0\text{-}\mu\text{m SiO}_2$, $\Delta\lambda \sim 70\text{ nm}$. The implantation conditions were: 1 MeV , P^+ at $200\text{ }^\circ\text{C}$ with annealing treatments performed at $700\text{ }^\circ\text{C}$ for 90 s .

The p-i-n laser structure used for this study was grown using metal-organic chemical vapor deposition (MOCVD). The active region consists of twelve 3.5-nm InGaAsP QW (emitting at $1.3\text{ }\mu\text{m}$) sandwiched between 10-nm InGaAsP barriers. Phosphorous implantation was performed at $200\text{ }^\circ\text{C}$ at an angle of 7° to the surface normal to minimize ion channeling. Subsequent rapid thermal anneals were performed at $700\text{ }^\circ\text{C}$ for 90 s with ramp rates of $20\text{ }^\circ\text{C/s}$ and with the implanted surface protected by a polished GaAs wafer. This thermal annealing cycle was selected to reduce the effect of strain on the full 50-mm InP wafer. An implant energy of 1 MeV was chosen to center the peak of the implantation induced damage at least $1\text{ }\mu\text{m}$ away from the active QW region. The dose was $1 \times 10^{14}\text{ cm}^{-2}$ at a constant flux of 120 nA/cm^2 . Different blue shifts were achieved by ion implanting through a SiO_2 mask of varying thicknesses as described in Section IV-B.

To monitor the compositional disordering on the patterned 50-mm wafer, a room temperature, two-dimensional map of the peak wavelength of the PL emission was measured as shown in Fig. 25. The optical excitation was provided by a CW Nd:YLF laser (1047 nm) at a power of 20 mW , focused down to a $25\text{-}\mu\text{m}$ diameter spot. The step size (i.e., spatial resolution) was set to $500\text{ }\mu\text{m}$ and the luminescence originating from the wafer was dispersed by a spectrometer with a spectral resolution of 1 nm . The PL map clearly shows four distinct regions as defined by the SiO_2 patterning prior to implantation. As expected, the magnitude of the blue shift in the PL emission correlates with the total number of defects generated in the laser structure. Where the SiO_2 mask was the thickest, i.e., the lower part of the wafer, no disordering (PL blue shift) took place and the peak of the PL emission was at $1.292\text{ }\mu\text{m}$. In the case where no SiO_2 mask was used,

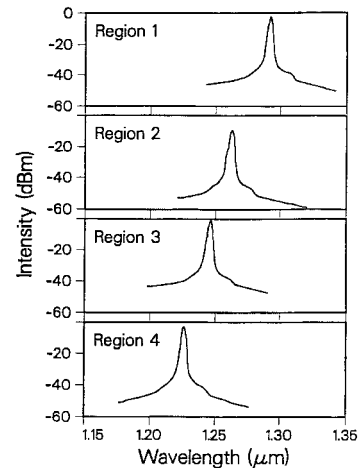


Fig. 26. Emission spectra of the bandgap shifted ridge waveguide lasers. No significant difference in threshold current ($20\text{--}25\text{ mA}$) or differential quantum efficiency ($0.25\text{--}0.30\text{ W/A}$) was observed from the four different implanted regions. The measured emission wavelengths from each of the four implanted regions are: 1.292 , 1.2629 , 1.2461 , and $1.2266\text{ }\mu\text{m}$ for regions 1–4, respectively.

(i.e., the upper part of the wafer) maximum interdiffusion was achieved and the PL emission was blue shifted by $\sim 70\text{ nm}$. One remarkable observation that can be made from this two-dimensional PL map is the uniformity obtained in the PL peak wavelength for a given mask thickness. This is somewhat surprising considering the fact that the wafer temperature uniformity during implantation was only $\sim 10\text{ }^\circ\text{C}$ and, as discussed in Section III-A, the substrate temperature during implantation is a very critical parameter in controlling the degree of interdiffusion of the QW's as well as controlling its crystalline quality [31]. The PL linewidth obtained from the four different regions did not increase significantly, as previously observed in a different laser structure operating at $1.55\text{ }\mu\text{m}$ [43]. Finally, the integrated PL intensity, which is strongly influenced by residual nonradiative recombination centers, did not decrease with increased disordering. This further demonstrates that the crystalline quality of the device can be maintained after interdiffusion.

Ridge waveguide laser diodes from each of the four regions of the center portion of the wafer were cleaved and tested. Approximately 30 device chips were cleaved from each bar and measured for light and voltage dependencies on drive current ($L\text{--}I$ and $V\text{--}I$), then mounted p-side down on diamond/copper blocks. Mounted chips were remeasured for $L\text{--}I$ and $I\text{--}V$ curves, then measured individually for spectral intensity vs. wavelength. Fig. 26 shows the lasing spectra from laser diodes from each of the four regions which have undergone different degrees of intermixing. No significant difference in threshold current ($20\text{--}25\text{ mA}$) or differential quantum efficiency ($0.25\text{--}0.30\text{ W/A}$) was observed from the four different implanted regions. These are the same values obtained from laser structures fabricated from the as-grown wafer which had not undergone any implantation or rapid thermal annealing. This indicates that the shifted laser material is of high quality, as any damage left in the active region of the device after implantation/anneal would add to the loss in the cavity and increase the threshold current. As was previously

reported, this observation suggest that factors contributing to changes in the threshold current such as alteration of the well shape, barrier height, and dopant diffusion in the active region and changes in the number of nonradiative recombination centers within the material are not significant [43].

The reliability of intermixed InGaAsP–InP QW lasers, which is of primary importance for any practical application, was tested in this study. Accelerated lifetime testing of devices obtained from the four intermixed regions was carried out at a temperature of 100 °C with a driving current of 150 mA for a period of 500 h. For devices from regions 1 and 2, the predicted device lifetime (based on 50% increase in current) for operation at 25 °C is in excess of 25 years (using 0.4 eV activation energy). This is currently used as a benchmark for standard (nonimplanted) devices. Devices from regions 3 and 4 exhibit higher and more random degradation rates and were deemed to be less reliable. Hence, for the present implantation and anneal conditions, active devices fabricated from material that is wavelength shifted up to ~35 nm were observed to be reliable. Further optimization of implantation temperature and annealing time (presently 200 °C and 90 s. respectively), may result in wavelength shifts greater than 35 nm while retaining 25 years predicted reliability of active devices.

D. Polarization Insensitive QW Modulator and Amplifier

It is well established that the performance of many semiconductor heterostructure optoelectronic devices such as lasers, optical amplifiers, and Stark effect modulators is enhanced through the incorporation of QW layers in their design. For example, it has been demonstrated that in QW optical amplifiers, quantum and differential quantum efficiencies, gain, and saturation output power are all increased [46]. However, active devices incorporating QW's have one major drawback; their performance is highly polarization sensitive due to the lifting of the degeneracy of the HH and LH valence bands at the Brillouin zone center by the quantum confinement effect. Thus, in a semiconductor waveguide containing QW's, the bandgap energy is a function of the polarization of the propagating beam with respect to the plane of the waveguide (labeled TE—transverse electric—or TM—transverse magnetic). In Fig. 27, the bandgap energy of a p-i-n QW waveguide is determined using wavelength dependent photoconductivity (which is equivalent to the absorption spectrum). Under an external bias of +1 V (which effectively cancels the built-in electric field of the p-i-n QW waveguide and produces the so-called flatband condition), the measured bandgap energy with TE polarized light is smaller (corresponding to a wavelength of about 1.555 μm) than that of TM polarized light (about 1.540 μm). TE light interacts with both the LH and HH valence bands while TM light only interacts with the higher energy LH band. Thus, the difference in bandgap energy as determined by TE and TM polarized light is a direct measure of the LH–HH valence band energy splitting in the QW. This waveguide structure, whether operated as a photodetector, quantum-confined Stark effect modulator, or optical amplifier would be quite sensitive to the signal polarization for wavelengths close to the bandgap, significantly degrading its performance

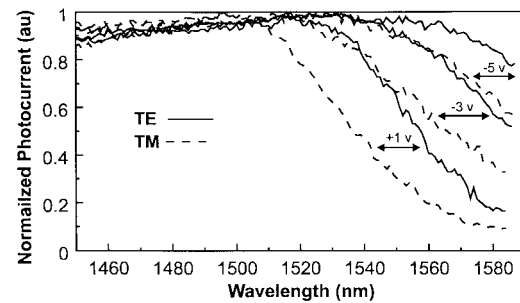


Fig. 27. Photocurrent (absorption) spectra of an as-grown, lattice matched InGaAs–InGaAsP QW waveguide as a function of external bias and for two orthogonal polarizations of the waveguide modes.

and usefulness. In contrast, bulk, unstrained, III–V zincblende semiconductor waveguide devices are polarization insensitive since their HH and LH bands are degenerate at the Brillouin zone. Clearly, in the best of all worlds, it would be very advantageous to have a waveguide device incorporating the benefits of a QW while simultaneously maintaining bulk-like polarization properties.

To achieve polarization insensitive optical amplification in a QW waveguide, several approaches have been demonstrated based on special geometric designs for active layers [47] or by the judicious incorporation of pseudomorphic strain [48]. Although some of these work quite well in eliminating polarization sensitivity of structures incorporating QW's, all of these require very sophisticated growth techniques and thus yield issues become important. Recently, ion induced QWI in a lattice matched InGaAs–InGaAsP MQW waveguide structure was shown capable of producing polarization insensitive semiconductor optical modulators and amplifiers operating in the 1.5- μm wavelength region. This technique is an appealing alternative due to its simplicity, since it is based on postgrowth modification of the structure.

For this paper, we again used the nominally unstrained laser structure shown schematically in Fig. 4. The high energy implantation conditions for this experiment were: Dose = $2.5 \times 10^{13} \text{ P}^+/\text{cm}^2$ at a substrate temperature of 200 °C with an energy of 1 MeV [13]. Here, again, the expected mean range of the ions (0.88 μm , according to the simulation program TRIM 91 [25]) was well short of the active region of the laser structure which is $\sim 1.7 \mu\text{m}$ beneath the surface. Again, different blue shifts were achieved by ion implanting through a SiO₂ mask of varying thicknesses as described in Section IV-B. The electrical characteristics of the as-grown and intermixed QW lasers were again essentially identical (see Fig. 20).

Fig. 27 presents the photocurrent spectra (essentially equivalent to the waveguide absorption spectra) of the as-grown InGaAs–InGaAsP QW waveguide structure as a function of the applied external bias and the polarization of the light. The output from a tunable external cavity diode laser was coupled into the waveguide via a tapered, polarization-maintaining fiber and the photocurrent was measured as a function of wavelength. Under zero internal electric field conditions (achieved with an external bias of +1 V), bandgap energies for both TE and TM polarizations can be readily determined as mentioned

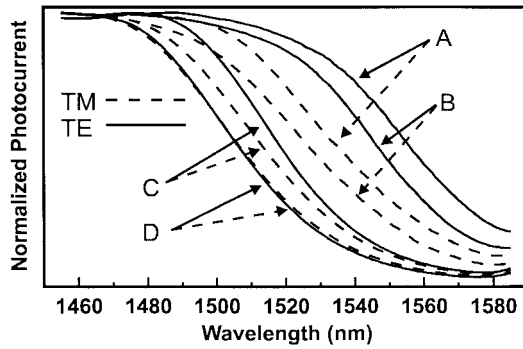


Fig. 28. Flatband photocurrent (absorption) spectra of intermixed quaternary QW waveguides as a function of the magnitude of QWI for two orthogonal light polarizations. TE: Solid lines. TM: Dashed lines.

previously. As the external bias is increased, these bandgaps red shift (to smaller energies, longer wavelengths) due to the quantum-confined Stark effect. These results are typical for semiconductor waveguides containing QW's and illustrate the large Stark shifts possible with QW structures due to the strong carrier confinement in quantum well layers. It also illustrates the polarization sensitivity of such QW waveguide photodetectors, modulators, etc.

When these QW's were intermixed using ion implantation enhanced interdiffusion, QW bandgaps increased, as expected and the LH-HH bandgap energy splitting decreased significantly. This is shown in Fig. 28, which illustrates the flat-band TE and TM bandgap energies for a series of QW waveguides with various amounts of QWI (A is as-grown (unmixed) and B to D correspond to increasing levels of QW shape modification). At a certain level of intermixing (D), the flatband LH-HH bandgap energy splitting is reduced to zero, to within experimental uncertainties, while the quantum-confined Stark effect is still operative, as demonstrated in Fig. 29. In this case the optical properties of the QW waveguide are polarization independent for most values of external bias. For larger internal electric fields, the valence band dependence of the Stark effect reintroduces a minor polarization dependence. But clearly, over a wide range of typical operating parameters, this QW waveguide structure performs in a polarization independent fashion.

Furthermore, the dependence of the bandgap energy on internal electric field is significantly enhanced in this intermixed QW waveguide, as can be determined by comparing Figs. 27 and 29. Fig. 30 illustrates this effect dramatically by plotting the TE and TM bandgap energies of as-grown and intermixed QW waveguides as a function of electric field. For an internal electric field of about 75 kV/cm, as-grown QW bandgaps are red-shifted by about 10 meV at best while intermixed QW's experience a decrease of about 50 meV. This significant enhancement of the quantum-confined Stark effect is due to the increased ability of the electric field to separate the electrons and holes in rounded QW's compared with QW's with "vertical" walls. Theoretical modeling confirms this explanation of the observations.

In any case, it is clear that QW intermixed waveguides can function as polarization independent photodetectors and as

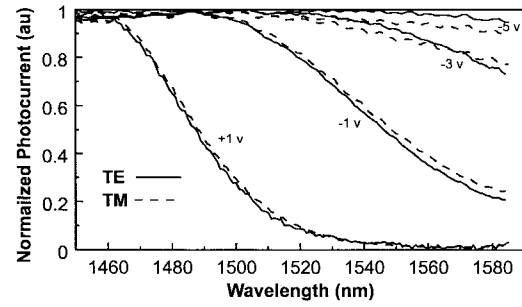


Fig. 29. Photocurrent (absorption) spectra of an intermixed quaternary QW waveguide as a function of external bias and for two orthogonal polarizations of the waveguide modes.

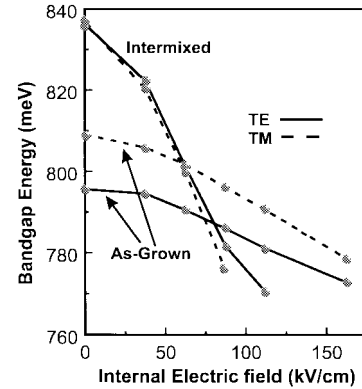


Fig. 30. Bandgap energy for as-grown and intermixed QW waveguides as a function of internal electric fields for light polarized in two orthogonal directions (TE and TM) with respect to the plane of the waveguide.

enhanced quantum confined Stark effect (electro-absorptive) modulators. Furthermore, in principle, the same technology (QW shape modification) can be used to monolithically integrate such devices together on a single wafer along with other active (e.g., lasers and optical amplifiers) and passive (transparent waveguides) structures.

Our understanding of this induced degeneracy of the TE and TM waveguide modes proceeds from the assumption that, after QW intermixing, lattice matched, nominally unstrained, InGaAs-InGaAsP QW's are strained in some complex manner due to the movement of group-III (Ga and In) and group V (As and P) atoms during the interdiffusion processes. This mechanism has been modeled by assuming different diffusion lengths, Δ_{III} or Δ_V , for the cations and anions [49], [50]. The parameter of importance is the ratio of diffusion lengths, $k = \Delta_V/\Delta_{III}$. Interdiffusion involving only one sublattice, or where the degree of interdiffusion on the group III and group V sublattices differs considerably ($\Delta_{III} \neq \Delta_V$), will result in the development of local strain in the QW region. The effect of interdiffusion on the energy band profile (including strain effects) and confined states for valence and conduction bands has been modeled using error function distributions for the anions and cations to predict compositional profiles that result after implantation and annealing [49], [50].

For a given QW structure, the LH-HH energy splitting as a function of HH energy can be calculated for various values of k and compared with experimental values obtained near

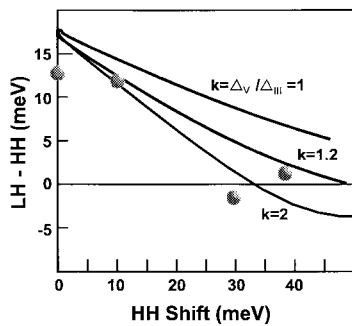


Fig. 31. Comparison of experimental HH-LH bandgap splitting as a function of heavy hole shift after implantation and annealing with theory for different interdiffusion length ratios, k . The experimental data points were obtained under flatband conditions.

flat-band conditions as shown in Fig. 31. From this analysis, it is clear that, within this model, our experimental data can only be explained by assuming $k > 1$. Scatter in the data and a decreasing sensitivity of LH-HH splitting on increasing k values preclude a more accurate determination of the ratio. For such values of k , a tensile strain develops at the QW center [49], [50]. Larger values of k lead to higher tensile strains. Furthermore, the same authors showed that in the early stages of interdiffusion, a significantly larger blue shift is expected for $k > 1$ than that for $k < 1$. Results for a model in which the QW is assumed to remain square and unstrained [51], are very similar to those shown for $k = 1$ and thus do not explain our data. It has been reported that in tensile strained QW's the LH-HH splitting can be reduced and even reversed for large values of strain [52], which acts on valence bands in an opposite direction to that of quantum confinement. However, to exactly balance the quantum confinement splitting with the negative splitting due to tensile strain requires precise control of strains (i.e., compositions) and QW thicknesses. In contrast, according to the model discussed above and our experimental data (as shown in Fig. 31), using QW intermixing to accomplish LH, HH degeneracy is a much easier task since the degeneracy, in this case, is not a very sensitive function of HH bandgap shift.

Finally, the performance of such polarization independent structures was studied when operated under extreme conditions, such as those experienced by semiconductor optical amplifiers which require large forward currents for population inversion. To investigate the optical amplification characteristics of this waveguide structure, signal gains for the TE and TM modes were measured as a function of wavelength. Light was coupled into, and out of, the waveguide while a fixed forward driving current density of 1.33 kA/cm^2 was applied to both the as-grown and intermixed devices. Fig. 32 shows that a maximum optical amplification of about 25–30 dB was determined for both polarization states in the waveguide containing as-grown QW's. However, in a behavior analogous to that observed in Fig. 27, the optical gain spectra for the TE and TM modes are significantly different due to the quantum confinement splitting of the HH and LH valence bands. On the other hand, in the intermixed QW waveguide, the optical gain spectra of the TE and TM modes overlap, a consequence of the degeneracy of the LH and HH valence bands. Also,

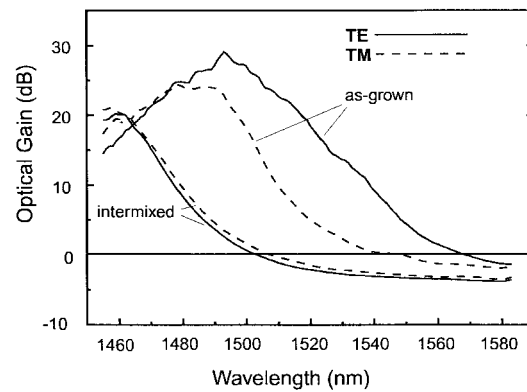


Fig. 32. Optical gain spectra for waveguides containing as-grown and intermixed InGaAs-InGaAsP QW's for two waveguide polarizations. TE: Dashed lines. TM: Solid lines.

the bandgaps for both TE and TM polarization modes were blue-shifted due to the QW shape modification effect. As a consequence, the optical gain spectra could only be determined down to about 1450 nm due to range limitations of our external cavity diode laser. But the important result is clear: the optical amplification of this waveguide structure containing the intermixed QW's is polarization insensitive, as expected.

To reiterate, we have shown that ion implantation induced QW intermixing can be used to fabricate polarization insensitive photonic devices such as photodetectors, quantum confined Stark effect modulators, and optical amplifiers in lattice matched InGaAs-InGaAsP-InP MQW laser structures.

E. Superluminescent Diodes

Superluminescent diodes (SLD's) with their broad spectral widths are the light source of choice for applications including fiber-optical gyroscopes [53] and fault location in fiber-optic cables [54]. One of the major advantages of the SLD is the low optical coherence length [55] due to its broad emission, which can lead to high sensitivity in these applications. Different approaches have been taken to broaden the spectral width of SLD's to further decrease the coherence length. These techniques have centered on the design of structures in which different regions of the device emit at different wavelengths, effectively merging more than one SLD into a single device. This has been realized by incorporating quantum wells (QW's) of different widths into the active region of the device [56], or by changing the QW bandgap along the length of the device using selective-area MOCVD [57] or shadow masked growth [58]. These can suffer from strong input current dependencies of the spectral width and position, which would have to be well controlled for use in real systems. A different approach is to use ion-implantation induced QWI to fabricate a broad spectral width SLD centered around $1.47 \mu\text{m}$ [59].

The QW bandgap in a standard semiconductor laser structure was modified by ion implantation through a SiO_2 mask of varying thickness (as described previously) allowing the tuning of the emission wavelength across a single device with micron spatial resolution in a single implantation step. The structure from which the SLD's were fabricated was the same one as shown in Fig. 4. Using this QWI technique the device

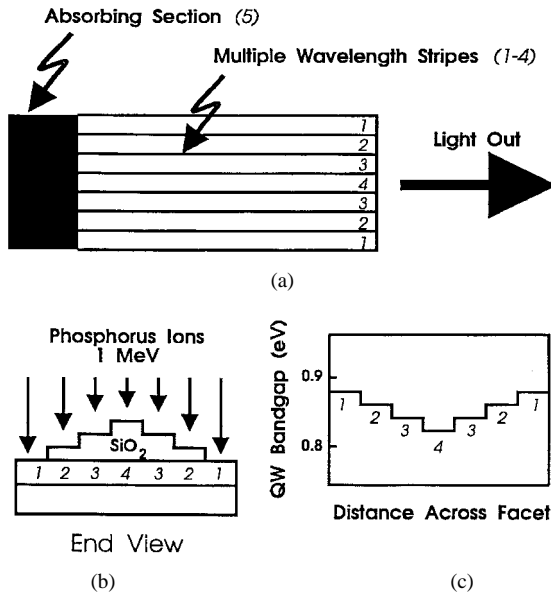


Fig. 33. A schematic diagram of the broad spectrum LED. (a) A top view showing the configuration of the multiple wavelength emitting stripes and the absorbing back section. (b) End view of the device with the SiO₂ ion-implantation mask in place. (c) Variation in QW bandgap energy across the multiple wavelength stripes after ion implantation and annealing. The regions marked 1–4 indicate the different thicknesses of SiO₂ used to mask the device during ion implantation.

shown in Fig. 33(a) was fabricated. It consists of seven parallel stripes which emit at a total of four different wavelengths, and a long absorbing section. The multiple wavelength stripes were made using the SiO₂ implantation mask shown in Fig. 33(b), with SiO₂ thickness of 0, 0.86, 1.15, and 1.44 μm , labeled 1–4 on Fig. 33. The 1.44 μm of SiO₂ was just thin enough to allow the 1-MeV P⁺ ions to reach the structure and provide a small wavelength shift after annealing. A thick layer of SiO₂ (2.1 μm) was used to block the P⁺ ions completely, region 5 on Fig. 33(a), to create the absorbing section. The bandgap variation across the stripes after implantation and annealing is shown schematically in Fig. 33(c). Due to the large decrease in the wavelength of the absorption edge between the as-grown and implanted material, the refractive index at long wavelength decreases by as much as 2.5% [35] after implantation. Hence, a symmetrical distribution of the different wavelength stripes about the center of the device was used to improve the waveguiding properties of the structure. Different stripe widths were used, with the optimum performance being observed with the regions 1–4 being 20, 5, 5, and 10 μm wide, respectively. After annealing, the devices were etched into ridges to improve their light guiding properties further, and gold contacts were evaporated covering the stripes (not the absorbing sections). The length of the gain region was 1000 μm with an absorbing region 1500 μm long.

The devices were tested using 1- μs pulses at a repetition frequency of 10 kHz and currents of up to 2 A. Fig. 34(a) shows the emitted spectra for pump currents of 1–2 A. As the current is increased the emitted power also increases, and a slight broadening of the spectrum to the blue is observed. The relative insensitivity of the spectral shape to drive current is a useful attribute, since any change in spectral output whilst

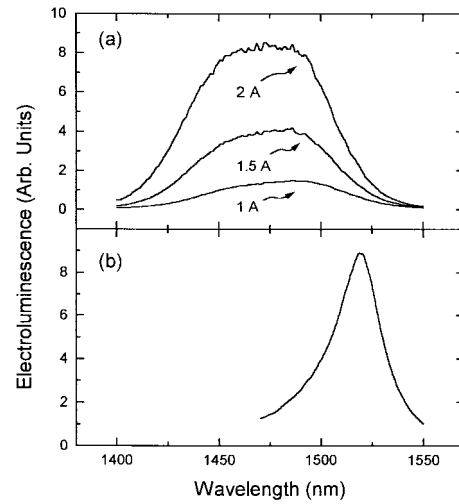


Fig. 34. (a) The output spectra for the device shown in Fig. 34 at different pump currents were regions 1–4 are 20, 5, 5, and 10 μm wide, respectively. The spectrum at 2 A has a FWHM of 90 nm centered around 1.47 μm . (b) The output spectrum for a conventional LED (100 $\mu\text{m} \times 1 \text{ mm}$ stripe) from the same material at a pump current of 900 mA. The FWHM of the emission for this device is only 28 nm.

operating will dramatically reduce its performance in sensing applications. The ripples on the spectra, particularly noticeable at a drive current of 2 A are due to water absorption. At a current of 2 A, the spectrum has a FWHM of 90 nm with a relatively flat top, the signal dropping only 10% over a 45-nm range, and an integrated power of 5 mW. This compares to a typical spontaneous emission width of 28 nm for a conventional LED from the same material, Fig. 34(b), an enhancement of over 60 nm.

A high-resolution scan showed no evidence of any Fabry–Perot modes implying that the absorber region was stopping any feedback from the cleaved back facet, i.e., it prevents an optical round-trip. Similar devices were fabricated without the absorption section, and were found to lase at long wavelength (1.5 μm) with a drive current of less than 700 mA. This demonstrates very clearly that the absorption section completely stops the device from lasing and removes Fabry–Perot noise from the emission spectrum. This allows a larger current to be passed through the device to generate more optical power. There was no need to apply antireflection coatings to the facets for device operation although a coating on the output facet would increase the light output by approximately 30%.

The widest spontaneous emission spectra were obtained when the total volume of each of the regions 2–4 were the same, and region 1 (the region emitting furthest to the blue) was four times as large. This is possibly due to improved waveguiding for the longer wavelengths in the device caused by the increasing bandgap as the edges of the device are approached. This creates a refractive index profile that helps guide the long wavelength emission. This is not the case for the shortest wavelength since it cannot enter the center of the device without being absorbed. Any light from the short wavelength region that is absorbed in regions 2–4 will also be reemitted at longer wavelength.

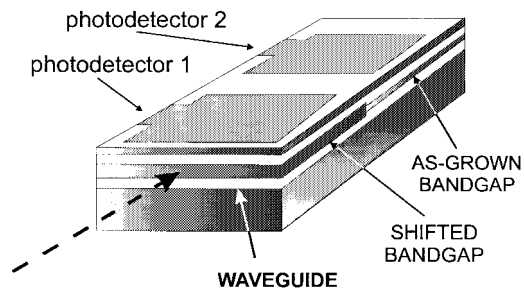


Fig. 35. Schematic diagram illustrating the principle of operation of a two-wavelength WDM DEMUX fabricated using QW intermixing.

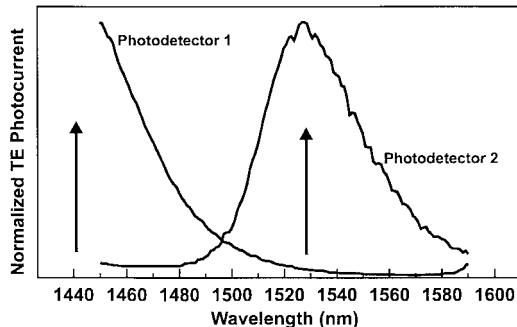


Fig. 36. Normalized room temperature TE photocurrent spectra of as-grown and intermixed regions of the two wavelength WDM demultiplexer shown schematically in Fig. 35.

F. Photodetector/Demultiplexer

Since the technique of ion-induced QW intermixing is simple to implement, and results in material of very high optical quality, many novel PIC's can be envisioned. An elementary example, a very simple two-wavelength demultiplexer, is shown in Fig. 35 [15]. It consists of two regions of a standard waveguide laser structure, one of which has been intermixed and one that has not. Light is coupled into the waveguide and passes through the intermixed into the nonintermixed region. Photons with a wavelength shorter than the bandgap of the first, blue-shifted, section will be absorbed in that region, generating a photocurrent. Longer wavelength light that is not absorbed in the first section will pass through to the as-grown region which has a smaller bandgap energy, and will be absorbed and detected there.

Fig. 36 presents the photocurrent spectra observed in each of the two regions as the wavelength of TE light from a tunable laser is scanned from 1.45 to 1.59 μm . Clearly each photodetector is sensitive to a different region of the optical spectra and so this device is able to distinguish between low (arrow at 1.53 μm) and high (arrow at 1.40 μm) energy photons. This device is extremely simple to fabricate and provides an elementary form of demultiplexing.

Other PIC's that could be fabricated using QWI would include laser-external modulators (as in Fig. 1), laser-rear-facet monitors, optical drops, and add-drops. However, more complex PIC's, such as optical switches, optical routers, multiple wavelength MUXes (which multiplex, or combine, optical signals of differing wavelengths) and DEMUXes (which demultiplex multiplexed optical signals) would be equally feasible.

V. SUMMARY

In conclusion, QWI processes offer a simple and potentially low cost route for fabricating PIC's. Optimized discrete devices will always possess the ultimate performance. The compromises inherent in any integration process (with the exception of the complex etch-and-regrow technique) make it impossible to optimize every device in a PIC. However, the advantages gained from integration in terms of reliability, cost and functionality compensate for any loss in individual device performance. QWI techniques have the potential to be high-yield and have now been demonstrated to meet the performance requirements of PIC's in terms of such parameters as propagation loss, retention of good electrical characteristics, enhanced QCSE, good reliability, lateral resolution, and lateral control of the degree of intermixing. Furthermore, QWI can provide the vital added benefit of polarization insensitivity for certain QW-based devices. Since the process is easy to implement, it will simplify the fabrication of many complex photonic integrated circuits and may finally render them practical.

REFERENCES

- [1] R. C. Alferness, U. Koren, L. L. Buhl, B. I. Miller, M. G. Young, T. L. Koch, G. Raybon, and C. A. Burrus, "Broadly tunable InGaAsP/InP laser based on a vertical coupler filter with 57 nm tuning range," *Appl. Phys. Lett.*, vol. 60, pp. 3209–3211, 1992.
- [2] E. S. Koteles, "Techniques for Monolithically Fabricating Photonic Integrated Circuits," in *Applications of Photonic Technology*, G. A. Lampropoulos, J. Chrostowski, and R. M. Measures, Eds. New York: Plenum, 1995, pp. 413–418.
- [3] A. R. Pratt, R. L. Williams, C. E. Norman, M. R. Fahy, A. Marinopoulou, and F. Chatenoud, "Indium migration control on patterned substrates for optoelectronic device applications," *Appl. Phys. Lett.*, vol. 65, pp. 1009–1011, 1994.
- [4] J. H. Marsh, "Quantum well intermixing," *Semiconductor Sci. Technol.*, vol. 8, pp. 1136–1155, 1993.
- [5] S. R. Andrew, J. H. Marsh, M. C. Holland, and A. H. Kean, "Quantum well laser with integrated passive waveguide fabricated by neutral impurity disordering," *IEEE Photon. Technol. Lett.*, vol. 4, pp. 426–428, 1992.
- [6] W. D. Laidig, N. Holonyak, M. D. Camras, K. Hess, J. J. Coleman, and P. D. Dapkus, and J. Bardeen, "Disorder of an AlAs-GaAs superlattice by impurity diffusion," *Appl. Phys. Lett.*, vol. 38, p. 776, 1981.
- [7] E. V. K. Rao, M. Juhel, P. Krauz, Y. Gao, and H. Thibierge, "Long range disordering of GaAs-AlGaAs multiple quantum wells by isoelectronic antimony implants," *Appl. Phys. Lett.*, vol. 62, pp. 2096–2098, 1993.
- [8] J. J. Dubowski, S. Charbonneau, A. P. Roth, P. J. Poole, C. Lacelle, M. Buchanan, I. V. Mitchell, and R. D. Goldberg, "A comparative study of laser- and ion implantation-induced quantum well intermixing in InGaAsP/InP microstructures," *SPIE Proc.*, 1997, vol. 2991, pp. 113–118.
- [9] D. G. Deppe, L. J. Guido, N. Holonyak, K. C. Hsieh, R. D. Burnham, R. L. Thornton, and T. L. Paoli, "Stripe-geometry quantum well heterostructure AlGaAs-GaAs lasers defined by defect diffusion," *Appl. Phys. Lett.*, vol. 49, pp. 510–512, 1986.
- [10] J. D. Ralston, S. O'Brien, G. W. Wicks, and L. F. Eastman, "Room temperature exciton electroabsorption in partially intermixed GaAs/AlGaAs quantum well waveguides," *Appl. Phys. Lett.*, vol. 54, pp. 534–536, 1989.
- [11] E. S. Koteles, B. Elman, R. P. Holmstrom, and P. Melman, "Modification of the shape of GaAs/AlGaAs quantum wells using rapid thermal annealing," *Int. J. Superlatt. Microstruct.*, vol. 5, pp. 321–325, 1989.
- [12] S. Charbonneau, P. J. Poole, P. G. Piva, G. C. Aers, E. S. Koteles, M. Fallahi, J. J. He, J. P. McCaffrey, M. Buchanan, M. Dion, R. D. Goldberg, and I. V. Mitchell, "Quantum well intermixing for optoelectronic integration using high energy ion implantation," *J. Appl. Phys.*, vol. 78, pp. 3697–3704, 1995.
- [13] P. J. Poole, S. Charbonneau, G. C. Aers, T. E. Jackman, M. Buchanan, M. Dion, R. D. Goldberg, and I. V. Mitchell, "Defect diffusion in ion im-

- planted AlGaAs and InP: Consequence for quantum well intermixing," *J. Appl. Phys.*, vol. 78, pp. 2367–2371, 1995.
- [14] P. Gavrilovic, D. G. Deppe, K. Meehan, N. Holonyak, and J. J. Coleman, "Implantation disorder of $\text{Al}_x\text{Ga}_{1-x}\text{As}$ superlattices," *Appl. Phys. Lett.*, vol. 47, p. 130–133, 1985.
 - [15] E. S. Koteles, S. Charbonneau, P. Poole, J. J. He, M. Davies, M. Dion, G. Aers, Y. Feng, I. V. Mitchell, and R. D. Goldberg, "Photonic integration using quantum well shape modification," *Phys. in Canada*, pp. 251–255, Sept./Oct. 1996.
 - [16] P. J. Poole, S. Charbonneau, M. Dion, M. Buchanan, J. J. He, E. S. Koteles, I. V. Mitchell, and R. Goldberg, "Quantum well intermixing for the realization of photonic integrated circuits," in *Emerging Components and Technologies for All-Optical Networks*, E. S. Koteles and A. E. Wilner, Eds., 1995, pp. 9–16.
 - [17] P. J. Poole, M. Buchanan, G. C. Aers, Z. R. Wasilewski, M. Dion, M. Fallahi, J. J. He, S. Charbonneau, E. S. Koteles, I. V. Mitchell, and R. D. Goldberg, "Transparent waveguides for WDM transmitter arrays using quantum well shape modification," in *SPIE, Components for Wavelength Division Multiplexing*, vol. 2402, pp. 115–122, 1995.
 - [18] J. Z. Wan, J. G. Simmons, and D. A. Thompson, "Bandgap modification in Ne^+ -ion implanted InGaAs/InP and InAsP/InP quantum well structures," *J. Appl. Phys.*, vol. 81, pp. 765–770, 1997.
 - [19] E. S. Koteles, A. N. M. Choudhury, A. Levy, B. Elman, P. Melman, M. A. Koza, and R. Bhat, "quantum well shape modification in quaternary quantum wells," in *Proc. Mater. Res. Soc. Symp.*, 1992, vol. 240, pp. 171–176.
 - [20] C. Vieu, G. B. Assayas, and J. Gierak, "Observation and simulation of focused ion beam induced damage," *Nucl. Instrum. and Meth.*, vol. B93, pp. 439–446, 1994.
 - [21] T. E. Jackman, S. Charbonneau, L. B. Allard, R. L. Williams, I. M. Templeton, M. Buchanan, M. Vos, I. V. Mitchell, and J. A. Jackman, "Compositional disordering of strained InGaAs/GaAs quantum wells by Au implantation: Channeling effects," *Appl. Phys. Lett.*, vol. 59, pp. 27–29, 1991.
 - [22] S. Charbonneau, P. J. Poole, P. G. Piva, G. C. Aers, E. S. Koteles, M. Fallahi, J.-J. He, J. P. McCaffrey, M. Buchanan, M. Dion, R. D. Goldberg, and I. V. Mitchell, unpublished.
 - [23] L. B. Allard, G. C. Aers, S. Charbonneau, T. E. Jackman, R. L. Williams, I. M. Templeton, and M. Buchanan, "Fabrication of nanostructures in strained InGaAs/GaAs quantum wells by focus ion beam implantation," *J. Appl. Phys.*, vol. 72, pp. 422–428, 1992.
 - [24] P. G. Piva, P. J. Poole, M. Buchanan, G. Champion, I. Templeton, G. C. Aers, R. Williams, Z. R. Wasilewski, E. S. Koteles, and S. Charbonneau, "Enhanced compositional disordering of quantum wells in GaAs/AlGaAs and InGaAs/GaAs using focused Ga^+ ion beam," *Appl. Phys. Lett.*, vol. 65, pp. 621–623, 1994.
 - [25] J. F. Ziegler, J. P. Biersack, and U. Littmark, *The Stopping and Ion Range of Ions in Matter*. New York: Pergamon, 1985.
 - [26] K. B. Kahen, D. L. Peterson, G. Rajeswaran, and D. J. Lawrence, "Properties of Ga vacancies in AlGaAs materials," *Appl. Phys. Lett.*, vol. 55, pp. 651–653, 1989.
 - [27] F. Laruelle, A. Bagchi, M. Tsuchiya, J. Merz, and P. M. Petroff, "Focused ion beam channeling effects and ultimate sizes of AlGaAs/GaAs nanostructures," *Appl. Phys. Lett.*, vol. 56, pp. 1561–1563, 1990.
 - [28] F. Laruelle, Y. P. Hu, R. Simes, W. Robinson, J. Merz, and P. M. Petroff, "Optical study of GaAs/AlGaAs quantum structures processed by high energy focused ion beam implantation," *Surf. Sci.*, vol. 228, pp. 306–309, 1990.
 - [29] R. D. Goldberg, I. V. Mitchell, P. J. Poole, D. Labrie, H. Lafontaine, G. C. Aers, R. Williams, M. Dion, and S. Charbonneau, "Ion beam intermixing of semiconductor heterostructure for optoelectronic applications," *Nucl. Instrum. Meth.*, vol. 127/128, pp. 418–422, 1997.
 - [30] R. D. Goldberg, P. G. Piva, I. V. Mitchell, P. J. Poole, S. Fafard, M. Dion, M. Buchanan, Y. Feng, and S. Charbonneau, "Conference on optoelectronic and microelectronic materials and devices," *Proc. IEEE*, pp. 118–121, 1997.
 - [31] U. G. Akano, I. V. Mitchell, F. R. Shepherd, and C. J. Miner, "temperature and dose dependence of damage production in Si^+ and Se^+ implanted InP," *Nucl. Instrum. Meth.*, vol. B106, pp. 308–315, 1995.
 - [32] R. D. Goldberg, J. S. Williams, and R. G. Elliman, "Amorphization of silicon by elevated temperature ion implantation," *Nucl. Instrum. Meth.*, vol. B106, p. 242, 1995.
 - [33] T. E. Haynes and O. W. Holland, "Dose rate effects on damage accumulation in Si^+ -implanted GaAs," *Appl. Phys. Lett.*, vol. 58, pp. 62–64, 1991.
 - [34] D. V. Forbes, J. J. Coleman, J. L. Klatt, and R. S. Averback, "Temperature dependence of ion-beam mixing in III–V semiconductors," *J. Appl. Phys.*, vol. 77, pp. 3543–3545, 1995.
 - [35] J. J. He, E. S. Koteles, P. J. Poole, M. Davies, R. Goldberg, I. Mitchell, and S. Charbonneau, "Bandgap shifted InGaAsP/InP quantum well waveguides using MeV ion implantation," *Electron. Lett.*, vol. 31, pp. 2094–2095, 1995.
 - [36] J. J. He, E. S. Koteles, M. Davies, P. J. Poole, S. Charbonneau, P. Piva, M. Buchanan, R. D. Goldberg, and I. V. Mitchell, "Transparency of bandgap shifted InGaAsP/InP quantum well waveguides," *Can. J. Phys.*, vol. 74, p. S32, 1996.
 - [37] N. K. Dutta, "Calculation of Auger rate in quantum well structure and its application to InGaAsP quantum well lasers," *J. Appl. Phys.*, vol. 54, pp. 1236–1245, 1983.
 - [38] J. E. Haysom, P. J. Poole, Y. Feng, E. S. Koteles, J.-J. He, S. Charbonneau, R. D. Goldberg, and I. V. Mitchell, "Lateral selectivity of ion-induced quantum well intermixing," *J. Vac. Sci. Technol.*, vol. A16, pp. 817–820, 1998.
 - [39] J. F. Ziegler, J. P. Biersack, and U. Littmark, *The Stopping Range of Ions in Solids*, J. F. Ziegler, Ed. New York: Pergamon, 1985.
 - [40] E. Kapon, N. G. Stoffel, E. A. Dobisz, and R. Bhat, "Birefringent channel waveguides defined by impurity-induced superlattice disordering," *Appl. Phys. Lett.*, vol. 52, pp. 351–353, 1988.
 - [41] J. E. Zucker, B. Tell, K. L. Jones, M. D. Divino, K. Brown-Groebeler, C. H. Joyner, B. I. Miller, and M. G. Young, "Large blue shifting of InGaAs/InP quantum well bandgaps by ion implantation," *Electron. Lett.*, vol. 60, pp. 3036–3038, 1992.
 - [42] J. E. Haysom, J. J. He, P. J. Poole, E. S. Koteles, A. Delage, Y. Feng, and S. Charbonneau, *J. Appl. Phys.*, submitted for publication.
 - [43] S. Charbonneau, P. J. Poole, Y. Feng, G. C. Aers, M. Dion, M. Davies, R. D. Goldberg, and I. V. Mitchell, "Bandgap tuning of InGaAs/InGaAsP/InP laser using high energy ion implantation," *Appl. Phys. Lett.*, vol. 67, pp. 2954–2956, 1995.
 - [44] J. Cibert and P. M. Petroff, "Carrier confinement potential in quantum well wires fabricated by implantation enhanced interdiffusion in the GaAs-AlGaAs system," *Phys. Rev.*, vol. B36, pp. 3243–3246, 1987.
 - [45] J.-P. Noël, D. Melville, T. Jones, F. R. Shepherd, C. J. Miner, N. Puetz, K. Fox, P. J. Poole, Y. Feng, E. S. Koteles, S. Charbonneau, R. D. Goldberg, and I. V. Mitchell, "High-reliability blue-shifted InGaAsP/InP lasers," *Appl. Phys. Lett.*, vol. 69, pp. 3516–3518, 1996.
 - [46] C. Weisbuch and B. Vinter, *Quantum Semiconductor Structures*. Boston, MA: Academic, 1991, ch. 23.
 - [47] I. Cha, M. Kitamura, H. Honmou, and I. Mito, "1.5 mm band travelling wave semiconductor optical amplifiers with window facet structure," *Electron. Lett.*, vol. 25, pp. 1241–1242, 1990.
 - [48] H. W. Wan, T. C. Chong, and S. J. Chua, "Considerations for polarization insensitive optical switching and modulation using strained InGaAs/InAlAs quantum well structure," *IEEE Photon. Technol. Lett.*, vol. 3, pp. 730–733, 1991.
 - [49] W.-C. Shiu, J. Micallef, I. Ng, and E. H. Li, "Effect of different cation and anion interdiffusion rates in disordered InGaAs/InP single quantum well," *Jpn. Appl. Phys.*, vol. 34, pp. 1778–1783, 1995.
 - [50] J. Micallef, E. H. Li, and B. L. Weiss, "Effect of interdiffusion on the sub-band-edge structure of InGaAs/InP single quantum well," *J. Appl. Phys.*, vol. 73, pp. 7524–7532, 1993.
 - [51] H. Temkin, S. N. G. Chu, M. B. Panish, and R. A. Logan, "Thermal stability of InGaAs/InP quantum well structures grown by gas source MBE," *Appl. Phys. Lett.*, vol. 50, pp. 956–958, 1987.
 - [52] F. Agahi, K. M. Lau, E. S. Koteles, A. Baliga, and N. G. Anderson, "GaAsP/GaAs quantum well structures with tensile-strained barriers," *IEEE J. Quantum Electron.*, vol. 30, pp. 459–466, 1994.
 - [53] W. K. Burns, C. L. Chen, and R. P. Moeller, "Fiber optic gyroscopes with broad-band sources," *J. Lightwave Technol.*, vol. LT-1, pp. 98–105, Jan. 1983.
 - [54] K. Takada, I. Yokohama, K. Chida, and J. Noda, "New measurement system for fault location in optical waveguide devices based on an interferometric technique," *Appl. Opt.*, vol. 26, pp. 1603–1606, 1987.
 - [55] Y. Noguchi, H. Yasaka, O. Mikami, and H. Nagai, "High-power broad band InGaAsP superluminescent diode emitting at 1.5 μm ," *J. Appl. Phys.*, vol. 67, pp. 2665–2667, 1990.
 - [56] O. Mikami, H. Yasaka, and Y. Noguchi, "Broader spectral width InGaAsP stacked active layer superluminescent diodes," *Appl. Phys. Lett.*, vol. 56, pp. 987–989, 1990.
 - [57] M. L. Osowski, T. M. Cockerill, R. M. Lammert, D. V. Forbes, D. E. Ackley, and J. J. Coleman, "A strained-layer InGaAs-GaAs-AlGaAs single quantum well broad spectrum LED by selective area MOCVD,"

in *LEOS'94 Conf. Proc. IEEE LEOS 7th Annu. Meet.*, 1994, vol. 1, pp. 119–120.

- [58] G. Vermeire, L. Buydens, P. Van Daele, and P. Demeester, “Side emitting GaAs/AlGaAs single quantum well LED's showing wide spectrum using shadow masked growth,” *Electron. Lett.*, vol. 28, pp. 903–905, 1992.
- [59] P. J. Poole, M. Davies, M. Dion, Y. Feng, S. Charbonneau, R. D. Goldberg, and I. V. Mitchell, “The fabrication of a broad spectrum light emitting diode using high energy ion implantation,” *IEEE Photon. Technol. Lett.*, vol. 8, pp. 1145–1147, 1996.

Sylvain Charbonneau, for a biography, see this issue, p. 745.

Emil S. Koteles (M'81), for photograph and biography, see this issue, p. 583.

P. J. Poole, photograph and biography not available at the time of publication.

J. J. He, photograph and biography not available at the time of publication.

G. C. Aers, photograph and biography not available at the time of publication.

J. Haysom, photograph and biography not available at the time of publication.

M. Buchanan, photograph and biography not available at the time of publication.

Y. Feng, photograph and biography not available at the time of publication.

A. Delage, photograph and biography not available at the time of publication.

F. Yang, photograph and biography not available at the time of publication.

M. Davies, photograph and biography not available at the time of publication.

R. D. Goldberg, photograph and biography not available at the time of publication.

P. G. Piva, photograph and biography not available at the time of publication.

I. V. Mitchell, photograph and biography not available at the time of publication.